

# DNS of Turbulent Flows Laden with Droplets or Bubbles

S. Elghobashi

Mechanical and Aerospace Engineering Department,  
University of California, Irvine, California 92689

Xxxx. Xxx. Xxx. Yyyy. AA:1–28

[https://doi.org/10.1146/\(\(please add article doi\)\)](https://doi.org/10.1146/((please add article doi)))

Copyright © Yyyy by Annual Reviews.  
All rights reserved

## Keywords

direct numerical simulation, turbulent multiphase flows, droplets, bubbles

## Abstract

**April 11, 2018- 14:10**

This review focuses on Direct numerical simulations (DNS) of turbulent flows laden with droplets or bubbles. DNS of these flows are more challenging than those of flows laden with solid particles due to the surface deformation in the former. The classification of the discussed numerical methods is based on whether the initial diameter of the bubble/droplet is smaller or larger than the Kolmogorov length scale, and whether the instantaneous surface deformation is fully resolved or obtained via a phenomenological model. Numerical methods that account for the breakup of single droplet/bubble as well as multiple droplet/bubble in canonical turbulent flows are also discussed.

## 1. INTRODUCTION

Turbulent flows laden with liquid droplets or gas/vapor bubbles (also known as turbulent dispersed multiphase flows) are ubiquitous in nature and engineering applications. In nature, examples include rain, waterfall mists, air bubbles in the upper ocean, and vapor bubbles in geysers. Engineering applications include liquid fuel sprays in all types of combustion engines, paint sprays, spray drying in the pharmaceutical industry as well as food processing, and water vapor bubbles in nuclear reactor cooling systems or those created by cavitation in the wakes of ship propellers, just to list a few.

Direct numerical simulations (DNS) of turbulent flows laden with droplets or bubbles are more challenging than DNS of solid particle-laden turbulent flows due to the shape deformation of the dispersed phase in the former. Accurate prediction of the deformation of the interface between the dispersed and continuous phases requires proper accounting of the effects of surface tension and the different viscosities and densities of the two phases in the governing equations of motion. A dimensionless measure of the ability of the carrier fluid motion to deform the immersed droplets or bubbles is the Weber number,  $We$ , which is the ratio of the inertial forces to surface tension forces. Qualitatively, large  $We$  values enhance the deformability whereas lower values reduce it. Another dimensionless measure is Ohnesorge number,  $Oh$ , which is the ratio of viscous to surface tension effects, and is related to  $We$  and Reynolds number of the bubble/droplet according to  $Oh = \sqrt{We}/Re$ . For a fixed  $Re$  the effects of changing  $Oh$  are similar to those of changing  $We$ .

The size of the droplets or bubbles in the reviewed studies ranges from smaller than to larger than the Kolmogorov length scale. In all the DNS studies reviewed here the governing conservation equations of the interacting fluid phases are solved on a fixed (Cartesian) grid. In other words, methods that use *interface-fitting adaptive grids* are not considered in this review since these methods considered only non-turbulent flows.

Since current supercomputers allow DNS to resolve only the turbulent fluid motion of length scales equal or greater than the Kolmogorov length scale, then it is not possible at present to fully resolve the motion of dispersed deformable sub-Kolmogorov scale droplets or bubbles. In order to overcome this difficulty, phenomenological models are used to compute the deformation of the dispersed phase as will be discussed in sections 2.1.2 and 3.1.2.

For deformable bubbles or droplets whose size is larger than the Kolmogorov length scale, the resolved shape and motion of the interface between the two phases are computed via one of the following *three* approaches:

### A. *Tracking points:*

Here the interface is marked by points that are advected by the flow as in the front tracking method of Unverdi & Tryggvason (1992) and Tryggvason et al. (2001).

### B. *Tracking scalar functions:*

Each of the following four numerical methods has its tracking function.

1. Volume of fluid (VOF), where the function is the volume fraction of the local phase on either side of the interface (Scardovelli & Zaleski (1999)).
2. Level Set (LS), where the function is the signed distance function representing the shortest distance from the interface (Sussman et al. (1994); Osher & Fedkiw (2001)) or its hyperbolic-tangent version (Desjardins et al. (2008)).
3. Lattice Boltzmann (LB), where the function  $f_i^n(\mathbf{x}, t)$  is the probability density function of finding a fluid particle of each fluid phase  $n$  at position  $\mathbf{x}$ , time  $t$ ,

and moving in the direction  $i$  of one of the discretized lattice velocity directions. The physical properties of the fluid such as the density or momentum are defined as moments of  $f_i^n(\mathbf{x}, t)$ . In the discretized LB method (LBM) the moments are evaluated by quadrature summation over all  $i$ . The interface between two phases is modeled by adding an extra force to the LB equilibrium velocity to represent the microscopic interaction between the two phases (e.g. surface tension or diffusivity) (Shan & Chen (1993)).

4. Phase Field model (PFM), where the function is the *scalar phase field*,  $\phi(\mathbf{x}, t)$ , also known as *order parameter*, which represents one of the physical properties (e.g. molar concentration) of a binary fluid mixture.  $\phi(\mathbf{x}, t)$  is mostly uniform in the bulk phases and varies smoothly over a *diffuse* finite-thickness interfacial layer. The transport of  $\phi(\mathbf{x}, t)$  is governed by the Cahn-Hilliard equation (Cahn & Hilliard (1959)) which accounts for the advection of  $\phi(\mathbf{x}, t)$  by the fluid velocity and the diffusion which equals  $\nabla \cdot [M(\phi)\nabla\mu_\phi]$ , where  $M(\phi)$  is the fluid mobility, and  $\mu(\phi)$  is the chemical potential which is defined in terms of the free energy  $f(\phi)$  of the fluid. In contrast to the above three methods, here the surface tension forces are replaced by a continuum model of  $f(\phi)$  (Jacqmin (1999)). Accordingly, the Navier-Stokes equations are modified by adding the forcing function ( $\mu\nabla\phi$ ) to represent the surface tension forces (Gurtin et al. (1996)). Recently, a hybrid LBM-PFM was used to simulate the dispersion of liquid droplets in isotropic turbulence (Komrakova et al. (2015)) as will be discussed in section 3.2.4.

- C. *Immersed boundary method (IBM) with interaction potential model (IPM)*: This hybrid IBM-IPM is a recently developed approach (Spandan et al. (2017a)) that couples the immersed boundary method (IBM) with a phenomenological *interaction potential model* (IPM) to simulate deformable droplets or bubbles in a turbulent flow. The dynamics of the interface deformation is modeled via a 3D spring network distributed over the surface of the immersed droplet (deTullio & Pascazio (2016)). The IPM is based on the principle of minimum potential energy where the total potential energy depends on the extent of deformation of the spring network. Modeling the spring network requires computing ad-hoc elastic constants which is done through a reverse-engineered approach. The IBM enforces the boundary conditions at the interface (e.g. the no-slip). A moving-least-squares (MLS) approximation (Vanella & Balaras (2009)) is used to reconstruct the solution in the vicinity of the immersed surface and to convert the Lagrangian forcing back to the Eulerian grid. MLS ensures constructing uniform Lagrangian grid elements on the immersed surface as it deforms. Spandan et al. (2018) used IBM-IPM to study the deformation of bubbles dispersed in a turbulent Taylor-Couette flow and the effect of their deformation on drag reduction. This study will be discussed in section 2.2.3.

Anderson et al. (1998) provides a historical review of the early studies by Poisson, Maxwell, Gibbs, Rayleigh and van der Waals on modeling the interface between two immiscible fluids.

When necessary the numerical methods will be briefly discussed. However, the focus here is not on the fine details of the different numerical algorithms but rather on the contributions of the different methods to advancing our understanding of the physics of the interactions between turbulence and droplets or bubbles. This review intends to comple-

ment the recent reviews of turbulent dispersed multiphase flows by [Balachandar & Eaton \(2010\)](#), bubble-laden turbulent flows by [Tryggvason et al. \(2013\)](#), and simulation methods of particulate flows by [Maxey \(2017\)](#).

The article proceeds as follows. Section 2 discusses DNS of bubble-laden turbulent flows, Section 3 discusses DNS of droplet-laden turbulent flows, and Section 4 provides concluding remarks.

### 1.1. Glossary

The following is a list of the acronyms used in this article:

EL: Eulerian Lagrangian  
FTM: Front Tracking Method  
IBM: Immersed Boundary Method  
IPM: Interaction Potential Model  
NS: Navier-Stokes  
PFM: Phase Field Model  
TF: Two-Fluid  
TKE: Turbulence Kinetic Energy  
VOF: Volume Of Fluid

## 2. DNS OF BUBBLE-LADEN TURBULENT FLOWS

The word ‘bubbles’ in this article refers to either *gas bubbles* or *vapor bubbles* since the mechanical aspects of their motion in liquid are the same except for the stronger effects of added mass in the latter ([Prosperetti \(2017\)](#)).

The length scale  $d$  will be used to denote the maximum size of the bubble. Thus, for a *spherical bubble* the length  $d$  equals the diameter. For an *ellipsoidal bubble*,  $d$  equals the length of the major axis. In the following sections, the discussion will consider bubbles whose size  $d$  is smaller than the Kolmogorov length scale,  $\eta$ , as well as bubbles with  $d > \eta$ . Figure 1 shows a list of the authors whose papers are reviewed in this article.

### 2.1. Bubbles of size smaller than the Kolmogorov length scale, $d < \eta$

Bubbles with  $d < \eta$  are generally referred to as microbubbles ([Madavan et al. \(1984\)](#) and [Druzhinin & Elghobashi \(1998\)](#)). DNS of microbubble-laden turbulence can be performed using the two-fluid (TF) approach or the Eulerian-Lagrangian (EL) approach. The EL approach is based on the point-particle assumption ([Elghobashi & Prosperetti \(2009\)](#), [Balachandar & Eaton \(2010\)](#)).

**2.1.1. Nondeformable spherical bubbles with  $d < \eta$ .** The equation of motion of a nondeformable spherical microbubble in a turbulent flow has been derived by [Druzhinin & Elghobashi \(1998\)](#), following the approach of [Maxey & Riley \(1983\)](#), for the conditions of  $d < \eta$ , neglecting the Basset and lift forces, and assuming  $\rho_b \ll \rho_f$ , where  $\rho_b$  and  $\rho_f$  are the densities of the bubble gas and surrounding fluid (liquid) respectively, as:

$$\frac{dV_i}{dt} = 3 \frac{DU_i}{Dt} + \frac{1}{\tau_b} (U_{i,\mathbf{x}_b} - V_i + W \delta_{iz}) , \quad 1.$$

where the bubble response time  $\tau_b$  and terminal velocity  $W$  are defined as

$$\tau_b = \frac{d^2}{36\nu} ; \quad W = 2\tau_b g . \quad 2.$$

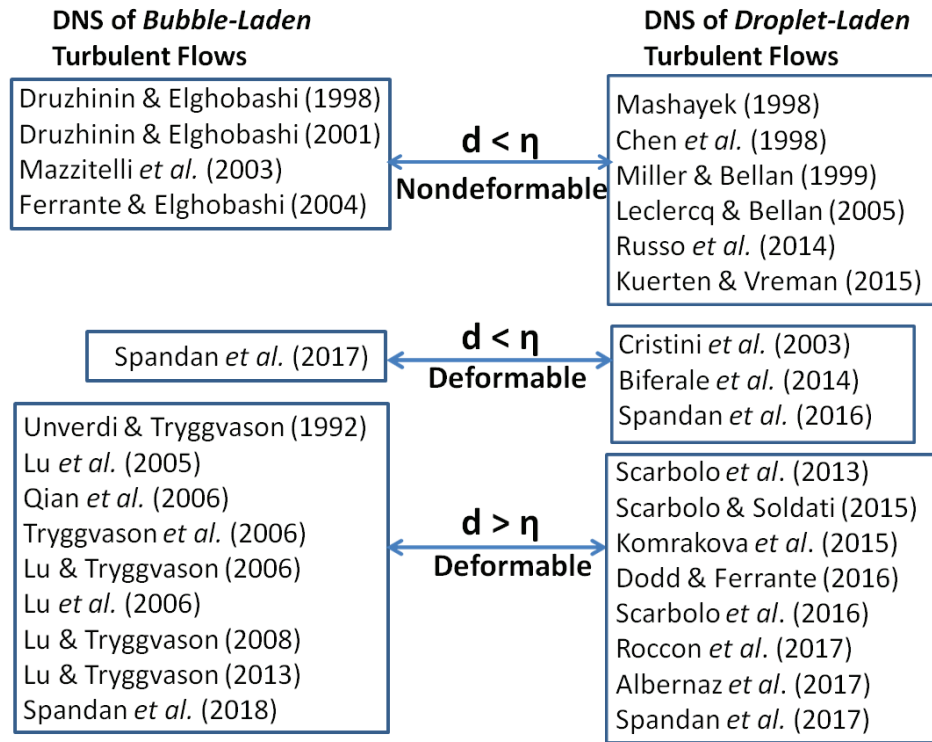


**Figure 1**

Reviewed DNS studies of bubble-laden and droplet-laden turbulent flows

In the above equations,  $V_i$  and  $U_i$  are respectively the instantaneous components of the bubble velocity and the carrier fluid velocity in the three coordinate directions.  $\mathbf{x}_b$  is the position of the bubble center,  $\frac{D}{Dt}$  is the Lagrangian derivative,  $g$  is the gravitational acceleration, and  $\nu$  is the kinematic viscosity of the carrier fluid. Eq.(1) is valid for the condition  $d < \eta$  which simultaneously *necessitates* that  $\tau_b < \frac{\tau_K}{36}$  according to Eq.(2), where  $\tau_K$  is the Kolmogorov time scale. This  $\tau_b$  condition for the bubble does not have a corresponding restriction for the solid particle when using the equation of Maxey & Riley (1983) where the particle response time,  $\tau_p$ , can be larger than  $\tau_K$ .

Druzhinin & Elghobashi (1998) derived the TF equations for a bubble-laden turbulent flow by spatially averaging the governing equations of the carrier fluid and the bubble phase over a scale of the order of  $\eta$ , which is much larger than the bubble diameter. They used the TF equations to predict a bubble-laden Taylor-Green vortex flow and decaying isotropic turbulence with two-way coupling. The same authors used the TF equations in DNS to study a 3D bubble-laden spatially developing mixing layer with two-way coupling Druzhinin & Elghobashi (2001).

Ferrante & Elghobashi (2007) performed DNS using the TF equations to study the effects of microbubbles on the vorticity dynamics in a Taylor-Green vortex flow. The results show that bubbles with a volume fraction  $\sim 10^{-2}$  enhance the decay rate of the vorticity at the center of the vortex. This is due to bubble clustering in the vortex core which creates

a positive velocity divergence. The vorticity transport equation shows that this positive  $\nabla \cdot \mathbf{U}$  enhances the local vorticity decay.

[Ferrante & Elghobashi \(2004\)](#) performed DNS of a microbubble-laden spatially developing turbulent boundary layer over a flat plate at  $Re_\theta = 1430$  to study drag reduction. They included the bubble lift force  $[(\mathbf{U} - \mathbf{V}) \times \boldsymbol{\Omega}_s]_i$  according to [Auton \(1987\)](#) and [Auton et al. \(1988\)](#) in Eq.(1), where  $\boldsymbol{\Omega}_s$  is the local vorticity vector. The lift force was needed for the bubble trajectories as they pass through the viscous sublayer where the fluid mean velocity gradient is maximum. The bubble diameter was  $d_b = 62 \mu\text{m}$ ;  $d_b^+ = 2.4$  in wall units, and volume fraction  $\Phi_v$  varied from 0.001 to 0.02.

The authors concluded that the presence of bubbles in the boundary layer results in a *local* positive divergence of the fluid velocity,  $\nabla \cdot \mathbf{U} > 0$ , creating a positive mean velocity normal to (and away from) the wall which, in turn, reduces the mean streamwise velocity and displaces the quasi-streamwise longitudinal vortical structures away from the wall. This displacement has two main effects: **1.** it increases the spanwise gaps between the wall streaks associated with the sweep events and reduces the streamwise velocity in these streaks, thus reducing the skin friction by up to 20.2% for  $\Phi_v = 0.02$ , and **2.** it moves the location of peak Reynolds stress production away from the wall to a zone of a smaller transverse gradient of the mean streamwise velocity (i.e. smaller mean shear), thus reducing the production rate of turbulence kinetic energy and enstrophy.”

The above described drag reduction mechanism applies for *nondeformable microbubbles* with  $d < \eta$ . We will discuss later in section 2.1.2 that drag reduction can be also realized by *deformable microbubbles* as well as *deformable large bubbles* with  $d > \eta$  in section 2.2.2.

[Mazzitelli et al. \(2003\)](#) performed DNS of microbubble-laden isotropic turbulence using the point particle approach to study the two-way coupling effects, especially that of the lift force discussed above. They used 144000 bubbles with  $d \sim 120 - 250 \mu\text{m}$  and volumetric fraction  $\Phi_v = 0.016$ . However, they applied artificial forcing to the turbulence kinetic energy (TKE) spectrum,  $E(k, t)$ , at small wavenumbers to create stationary turbulence at a fixed  $Re_\lambda = 62$ . This forcing ‘camouflages’ the true two-way coupling effects of the bubbles on the flow and thus *no correct* conclusion can be made about these effects. The *camouflage* is explained by the spectral transport equation of  $E(k, t)$ :

$$\frac{dE(k, t)}{dt} = T(k, t) - \varepsilon(k, t) + \Psi_b(k, t) + F(k, t), \quad 3.$$

where the terms on the RHS are respectively the transfer rate of TKE at wavenumber  $k$ , the dissipation rate, the bubbles two-way coupling rate, and the artificial forcing rate. The instantaneous two-way coupling and transfer rates (after omitting the  $t$ ) are:

$$\Psi_b(k) = - \sum_{\kappa \leq |\boldsymbol{\kappa}| < \kappa+1} \Re \left\{ \left\langle \hat{u}_j^*(\boldsymbol{\kappa}) \hat{f}_j(\boldsymbol{\kappa}) \right\rangle \right\}, \quad 4.$$

$$T(\kappa) = \sum_{\kappa \leq |\boldsymbol{\kappa}| < \kappa+1} \kappa_l P_{jk}(\boldsymbol{\kappa}) \Im \left\{ \sum_{\boldsymbol{\kappa}'} \left\langle \hat{u}_k(\boldsymbol{\kappa}') \hat{u}_l(\boldsymbol{\kappa} - \boldsymbol{\kappa}') \hat{u}_j^*(\boldsymbol{\kappa}) \right\rangle \right\}, \quad 5.$$

where  $\Re \{ \}$  and  $\Im \{ \}$  denote the real and imaginary parts, and

$$P_{jk}(\boldsymbol{\kappa}) \equiv \delta_{jk} - \frac{\kappa_j \kappa_k}{\kappa^2} \quad 6.$$

is the projection tensor, and  $\delta_{jk}$  is Kronecker delta.  $\hat{f}_j(\boldsymbol{\kappa})$  is the Fourier coefficient of the force  $f_j$  imparted by the bubbles on the surrounding fluid, and  $*$  denotes the com-

plex conjugate. The RHS of both (4) and (5) create nonlinear triadic interactions involving *all* wavenumbers of  $E(k, t)$  including the small wavenumbers where  $F(k, t)$  is applied (Ferrante & Elghobashi (2003)). These triadic interactions are responsible for *signaling* the effects of the perturbations created by the microbubbles at high wavenumbers to the large scales (small wavenumbers) (Elghobashi & Truesdell (1993)). Therefore, artificially increasing  $E(k, t)$  at small wavenumbers by  $F(k, t)$  *opposes* the two-way coupling effects of the microbubbles. Furthermore, by definition,  $\int_{k_{min}}^{k_{max}} \frac{dE(k, t)dk}{dt} = \frac{dE}{dt} = 0$  for a forced stationary turbulence and thus an invariant  $E(t)$  cannot show *any effects* of the two-way coupling. It is important to note that it is appropriate to use forced isotropic turbulence to study the dispersion of bubbles or particles in *one-way coupling* (e.g. Wang & Maxey (1993); Snyder et al. (2007)).

**2.1.2. Deformable bubbles with  $d < \eta$ .** Performing DNS of turbulent dispersed multiphase flows to resolve the shape deformation of millions of bubbles or droplets with  $d < \eta$  is beyond the capabilities of current parallel supercomputers. However, it is feasible to use the point particle approach combined with a phenomenological subgrid model to calculate the shape deformation of the dispersed phase. The first study (and the only one at present) that followed that approach is by Spandan et al. (2017b) and thus will be described here in some detail. Spandan et al. (2017b) performed DNS to study the flow of deformable sub-Kolmogorov bubbles dispersed in a turbulent Taylor-Couette flow. They used two-way coupled point-particle approach and were able to simulate approximately  $10^5$  continuously deforming bubbles. The density ratio,  $\hat{\rho}$ , of the bubble gas density to that of the liquid was  $10^{-3}$ , the viscosity ratio  $\hat{\mu}$  was  $10^{-2}$  and the volume fraction of the bubbles was  $\Phi_v = 10^{-3}$ . The study focused on the effect of deformability of bubbles on the reduction of the torque required to rotate the inner cylinder at a prescribed angular velocity. The reduction of the required torque is calculated by comparing the average shear stress at the rotating wall for the bubble-laden flow with that of a single-phase flow. The rotation rate of the inner cylinder was quantified by the inner cylinder Reynolds number,  $Re_i = r_i \omega_i (r_o - r_i) / \nu$ , where  $r_i, r_o, \omega_i$  and  $\nu$  are respectively the inner and outer cylinders radii, the angular velocity of the inner cylinder, and the kinematic viscosity of the carrier fluid. Two cases were simulated with  $Re_i = 2.5 \times 10^3$  and  $8 \times 10^3$ .

The bubble shape was assumed to be at all times a tri-axial ellipsoid described by a symmetric, positive definite second-rank tensor  $\mathbf{S}$  which satisfies the condition  $\mathbf{S}^{-1} : \mathbf{x}\mathbf{x} = 1$ , where  $\mathbf{x}$  is the position vector of any point on the ellipsoid surface relative to its center. The time rate of change of  $\mathbf{S}$  is described by the phenomenological equation of Maffettone & Minale (1998) which was originally developed for liquid droplets:

$$\frac{d\mathbf{S}}{dt} - \left[ \boldsymbol{\Omega} \cdot \mathbf{S} - \mathbf{S} \cdot \boldsymbol{\Omega} \right] = -\frac{f_1}{\tau} \left[ \mathbf{S} - g(\mathbf{S})\mathbf{I} \right] + f_2 \left[ \mathbf{E} \cdot \mathbf{S} + \mathbf{S} \cdot \mathbf{E} \right], \quad 7.$$

where  $\tau = \mu R / \sigma$  is the interfacial time scale,  $\mu$  is the dynamic viscosity of the carrier fluid (liquid),  $R$  is the radius of the equivalent undeformed spherical bubble, and  $\sigma$  is the surface tension.  $\mathbf{E}$  and  $\boldsymbol{\Omega}$  are the strain rate and rotational rate tensors respectively.  $\mathbf{I}$  is the second rank unit tensor.

The LHS of (7) is the Jaumann corotational derivative (Gurtin et al. (2010)) which is frame-invariant and depends on  $\boldsymbol{\Omega}$ . Equation(7) states that the temporal evolution of the *shape tensor*  $\mathbf{S}$  is governed by two competing phenomena: the interfacial tension (first term on the RHS) which attempts to restore the initial spherical shape, and the drag exerted by

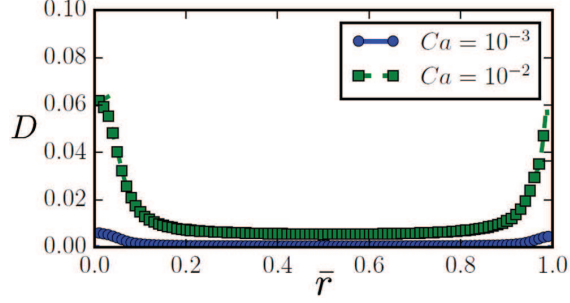


**Figure 2**

Radial (wall-normal) profiles of azimuthally-, axially- and temporally-averaged deformation parameter  $D$  of the sub-Kolmogorov length scale bubbles for two Capillary numbers, at  $Re_i = 2500$ . Source: [Spandan et al. \(2017b\)](#) with permission from the American Physical Society.

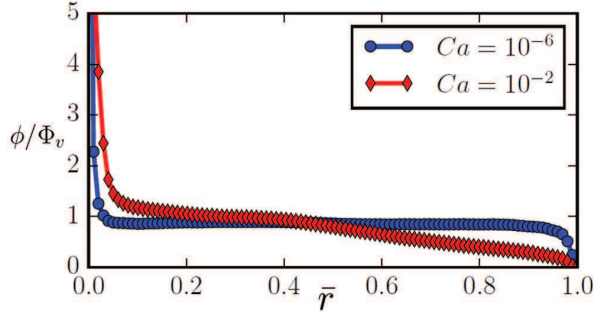


**Figure 3**

Radial (wall-normal) profiles of azimuthally-, axially- and temporally-averaged local volume fraction of the sub-Kolmogorov length scale bubbles,  $\phi$ , normalized by the total volume fraction,  $\Phi_v$ , for two Capillary numbers, at  $Re_i = 2500$ . Source: [Spandan et al. \(2017b\)](#) with permission from the American Physical Society.

the motion of the ellipsoid (second term on the RHS) while preserving the initial volume. The positive dimensionless coefficients  $f_1$  and  $f_2$  are functions of the viscosity ratio  $\hat{\mu}$ . The function  $g(\mathbf{S})$  is introduced to preserve the bubble volume and is proportional to the ratio of the third invariant of  $\mathbf{S}$  to the second invariant of  $\mathbf{S}$ . The derivation of (7) is given by [Maffettone & Minale \(1998\)](#).

Time integration of (7) leads to three eigenvalues of  $\mathbf{S}$  which equal the squares of the three semi-axes of the ellipsoid, and three eigenvectors that provide the orientations of the semi-axes. Equation(7) has been validated experimentally by [Guido et al. \(2000\)](#) for a neutrally buoyant liquid droplet immersed in a viscous fluid subjected to uniform shear.

[Spandan et al. \(2017b\)](#) assumed a small Capillary number which measures the relative importance of the viscous forces to surface tension forces at the small scale motion.  $Ca = \tau/\tau_K = (\eta\mu_f)/(\sigma\tau_K) \ll 1$ , where  $\mu_f$  is the dynamic viscosity of the carrier fluid and  $\tau_K$  is the Kolmogorov time scale. They further assumed that  $Ca_{max} = 0.1$  to ensure that the deformed ellipsoidal bubble is nearly axisymmetric. They used the drag and lift coefficients



developed by Njobuenwu & Fairweather (2015) for *solid* ellipsoidal particles by assuming that the bubble interface is contaminated with surfactants to satisfy the no-slip boundary condition. Lohse (2017) justified using the no-slip boundary condition for the bubble surface and the drag and lift forces for solid ellipsoids by setting  $Ca \ll 1$  and  $\hat{\mu} = 10^{-2}$ ; hence the viscosity of the bubble gas was negligible, thus minimizing the drag due to the internal gas circulation. The bubble acceleration equation accounted for the forces due to drag, lift, added mass and buoyancy.

The DNS results show that an increase in the deformability of the sub-Kolmogorov bubbles enhances drag reduction due to a significant accumulation of the deformed bubbles near the rotating inner wall (Figs. 2 and 3). In Figure 2 the dimensionless *deformation parameter* is  $D = (d_3 - d_1)/(d_3 + d_1)$  (Maffettone & Minale (1998)), where  $d_1$  and  $d_3$  are the lengths of the minor and major semi-axes of the ellipsoid, respectively. A larger concentration of bubbles near the driving wall indicates that they are effective in suppressing the plumes ejection process; hence drag reduction is greater. These plumes are unsteady vortical structures that detach from either the inner or outer cylinder in wall-normal direction (van der Veen et al. (2016)). The plume ejection occurs predominantly at the stagnation regions (along the walls) between the counter rotating rollers where a negative pressure gradient normal to the wall is created. The bubbles preferential accumulation is induced by increased resistance to the bubbles leaving the wall in its normal direction. The increased resistance is due to the strong deformation of the bubbles near the rotating wall which makes them prolate (stretched along one axis) and oriented along the streamwise direction.

## 2.2. Bubbles of size larger than the Kolmogorov length scale, $d > \eta$

### 2.2.1. Single bubble deformation and breakup in isotropic turbulence using LBM.

Qian et al. (2006) studied the deformation and breakup of a single bubble in stationary isotropic turbulence ( $20 \leq Re_\lambda \leq 35$ ) using LBM with D3Q15 lattice (cf. section 3.2.1) and the BGK (Bhatnagar et al. (1954)) form of the LB equation with single relaxation time. A validation test was made for a non-turbulent flow by comparing the results of this LBM with those of FTM for a 2D rising bubble and good agreement was achieved (Sankaranarayanan et al. (2003)). Qian et al. (2006) defined Weber number as  $We = \rho_l \langle \delta u^2 \rangle d_e / \sigma$ , where  $\delta u$  is the velocity difference over a distance equal to the bubble equivalent spherical diameter,  $d_e$ , and  $\langle \dots \rangle$  denote averaging over space and time. The results show that prior to bubble breakup, an increase in the bubble surface area by at least 37% occurs. They compared their results with the experimental data of Risso & Fabre (1998) which were conducted in a microgravity environment. Both the experiment and LBM indicate that a Weber number can be identified below which breakup is not observed. This Weber number is based on the statistics of the single-phase flow that would exist in the absence of the bubble. In LBM, this Weber number was approximately 3.0.

### 2.2.2. Deformable bubbles with $d > \eta$ in turbulent channel flow using FTM.

Unverdi & Tryggvason (1992) introduced the *front-tracking method* (FTM) in which one set of the incompressible Navier-Stokes and continuity equations is used for the whole computation domain, including the bubbles and the carrier liquid:

$$\rho \frac{\partial \mathbf{u}}{\partial t} + \rho \nabla \cdot \mathbf{u} \mathbf{u} = -\nabla P + \nabla \cdot \mu (\nabla \mathbf{u} + \nabla \mathbf{u}^T) + \sigma \int_F k_f \mathbf{n}_f \delta(\mathbf{x} - \mathbf{x}_f) dA_f, \quad 8.$$

$$\nabla \cdot \mathbf{u} = 0, \quad 9.$$

where  $\mathbf{u}$  is the velocity,  $P$  is the pressure, and  $\rho$  and  $\mu$  are the discontinuous density and viscosity fields, respectively.  $\delta$  is a three-dimensional delta function.  $\sigma$  is the surface tension coefficient,  $k$  is twice the mean curvature, and the subscript  $f$  denotes the ‘front’.  $\mathbf{n}$  is a unit vector normal to the front. The integral is over the entire front such that it creates a force acting at the interface but smooth along the front.  $\mathbf{x}$  is the point at which the equation is solved and  $\mathbf{x}_f$  is the position of the front.

The moving interface (front) between the bubble gas and the surrounding liquid is represented by unstructured mesh that explicitly marks the position of the front. The front mesh (or *marker*) points are advected by the carrier flow velocities, interpolated from the fixed Cartesian mesh. As the front deforms, surface markers are dynamically added or removed. An indicator function  $\mathbf{I}(\mathbf{x})$  which has the values 1 inside the bubble and 0 in the carrier liquid is constructed from the known position  $\mathbf{x}_f$ . Since both  $\rho$  and  $\mu$  are constant within each fluid, their values at any point can be calculated using  $\mathbf{I}(\mathbf{x})$ :  $\rho(\mathbf{x}) = \rho_0 + (\rho_b - \rho_0)\mathbf{I}(\mathbf{x})$ , and  $\mu(\mathbf{x}) = \mu_0 + (\mu_b - \mu_0)\mathbf{I}(\mathbf{x})$ , where the subscripts  $b$  and 0 denote the bubble and carrier fluids respectively.

To avoid numerical instabilities associated with a sharp interface, the front is given a thickness of the order of several mesh cells. In this narrow transition zone the fluid properties change smoothly. The sharp delta functions in (8) are approximated by smoother functions with a compact stencil on the fixed Cartesian mesh. At each time step, after the front has been advected, the density and the viscosity fields are reconstructed by integration of the smooth grid delta function. The surface tension force (last term on the RHS of (8)) is then added to the nodal values of the discretized Navier-Stokes equations. More details are given by Tryggvason et al. (2006).

Lu et al. (2005) performed DNS of a turbulent flow in a ‘minimum channel’ at  $Re_\tau = 135$ . They used the front tracking method (FTM) described above to study the effect of 16 dispersed bubbles on the wall shear stress. The nondeformed bubble diameter was 54 wall units. The density ratio was restricted to  $\rho_b/\rho_0 = 0.1$  and dynamic viscosity ratio  $\mu_b/\mu_0 = 1$  which resulted in the kinematic viscosity ratio  $\nu_b/\nu_0 = 10$ , a typical value for air bubbles in liquid water. Three Weber numbers,  $We = 0.203, 0.270$  and  $0.405$ , were tested. The results show that deformable bubbles (with largest  $We$ ) can lead to significant reduction of the wall drag by suppression of streamwise vorticity. Less deformable bubbles, on the other hand, are slowed down by the viscous sublayer and lead to a large increase in drag. The reduction of streamwise vorticity occurs by bubbles moving parallel to the wall at a distance of about one bubble radius between the bubble surface and the wall. These bubbles move over the streamwise vortices with a higher velocity than the advection velocity of the vortices. The passing of the bubbles forces the streamwise vortices closer to the wall, causing mutual cancelation between the streamwise vortices and the wall-bounded vorticity of the opposite sign. This results in a reduction of the streamwise vorticity and a corresponding reduction of the  $\overline{uv}$  component of the Reynolds stress tensor. Tryggvason et al. (2006) discuss the numerical difficulties that arise when using FTM with large density and viscosity ratios.

Lu & Tryggvason (2006) performed DNS with FTM to study a bubbly vertical channel *downflow* at  $Re_\tau = 127$ . The number of bubbles ranged from 18 to 72, and diameter =  $0.25H$ , with an average volume fraction ranging from  $0.015 \leq \Phi_v \leq 0.06$ , where  $H$  is half the channel width. The density and kinematic viscosity ratios were respectively  $\rho_b/\rho_0 = 0.1$  and  $\nu_b/\nu_0 = 10$ . The results show that the lift force on the bubbles near the wall caused them to concentrate in the core region and create a bubble-free wall layer.

Lu & Tryggvason (2008) performed DNS with FTM to study the effect of deformability of 21 bubbles on their dispersion in a turbulent bubbly *upflow* in a vertical channel at friction Reynolds number,  $Re_\tau = 127$ . The density and viscosity ratios were prescribed as those in Lu & Tryggvason (2006). Two cases were studied for two values of *Eötvös* number,  $Eu = \rho_f g d^2 / \sigma$ , which measures the ratio of gravitational forces to surface tension forces;  $Eu = 0.45$  for nearly spherical bubbles and 4.5 for deformable bubbles. The lift force on a clean spherical bubble rising in a vertical shear flow is directed toward the side where the fluid moves faster past the bubble, in a frame of reference moving with the bubble (Lu et al. (2006)) according to Saffman (1965). In channels, where the fluid velocity is zero at the walls, *spherical* bubbles will therefore move laterally toward the walls for upflow and away from the walls in downflow. However, bubble deformation can reverse the sign of the lift force. Furthermore, the lift force on strongly deformable bubbles is weaker than that on nearly spherical bubbles. Turbulent dispersion of deformable bubbles overcomes their tendency to concentrate in the core region of this upflow.

Lu & Tryggvason (2013) performed DNS of *nearly spherical bubbles* in a vertical turbulent channel upflow similar to their earlier study (Lu & Tryggvason (2008)) but at higher Reynolds number,  $Re_\tau = 250$ , and 140 bubbles. The bubble diameter was prescribed equal to 40 wall units = 0.08 of the channel width. At statistically steady state, the weight of the bubble-laden liquid and the imposed pressure gradient are balanced by the shear stress. For the upflow in the channel, as the bubbles migrate toward the wall (by the lift force) the average mixture density *in the core* increases until the weight is balanced exactly by the pressure gradient. The shear and subsequently the lift force vanish in the core region, thus ending the bubbles migration to the wall. As a result, the velocity gradient exists only in the wall region where the bubbles volume fraction reaches its peak (see Figs. 3 and 4 in Lu & Tryggvason (2013)). The high concentration of the bubbles in the wall layer results in a significant reduction of the turbulence kinetic energy and its dissipation rate there. However, Fig. 5 of Lu & Tryggvason (2013) also shows that the *peak of the dissipation rate* increases, as compared to single-phase flow, very close to the wall. The reason for that increase was not discussed in that reference.

### 2.2.3. Deformable bubbles with $d > \eta$ in turbulent Taylor-Couette flow using IBM-IPM.

Spandan et al. (2018) performed DNS to study the effects of dispersed deformable bubbles, with  $d > \eta$ , on drag reduction in a turbulent Taylor-Couette (TC) flow using a hybrid IBM-IPM (section 1). The surface of each dispersed bubble was discretized using an unstructured Lagrangian mesh. The effect of the bubbles on the carrier fluid is accounted for via a volume-averaged force computed on that mesh and then is transferred to the Eulerian mesh where the NS equations are solved. The deformation of the immersed bubbles is computed via the IPM where the surface tension of a liquid-gas interface is modeled using a triangulated network of elastic and torsional springs as described by Spandan et al. (2017a). Two cases were simulated with inner cylinder Reynolds number  $Re_i = 5 \times 10^3$  and  $2 \times 10^4$ . The number of the dispersed bubbles was 120, each with an initial diameter  $d_b \sim 14\eta$  and  $d_b \sim 25\eta$ , for the low and high  $Re_i$  cases, respectively, and a global volume fraction  $\Phi_v = 0.001$ . Each bubble was initialized as a sphere with its surface discretized with 1280 Lagrangian marker points for the low  $Re_i$  case, and 2560 markers for the high  $Re_i$  case. Four values of Weber number, based on the velocity of the inner cylinder, were considered:  $We = 0.01, 0.5, 1, 2$ . These values were assumed to be small enough to avoid bubble breakup or coalescence. The ratio,  $\hat{\rho}$ , of the bubble gas density to that of the liquid was  $5 \times 10^{-2}$ .

Bubble-bubble and bubble-wall collisions were modeled via elastic potential between the Lagrangian mesh nodes and the center of the enclosing Eulerian cell.

The results show that for all four  $We$  values the bubbles concentrate near the inner cylindrical wall. This is in contrast to the deformable sub-Kolmogorov bubbles which preferentially concentrate near the inner wall as  $We$  is increased (cf. section 2.1.2).

The drag reduction of the bubble-laden TC flow was derived by Sugiyama et al. (2008) as the sum of two terms :  $DR_1 = \left(1 - \frac{\langle \varepsilon_B \rangle}{\langle \varepsilon \rangle}\right)$  and  $DR_2 = \left(\frac{\langle \mathbf{f}_b \cdot \mathbf{u} \rangle}{\langle \varepsilon \rangle}\right)$ , where  $\langle \varepsilon_B \rangle$  and  $\langle \varepsilon \rangle$  are the mean dissipation rates of TKE per unit mass of the bubble-laden carrier fluid and the single-phase flow, respectively. The volume-averaged source term in NS equations,  $\mathbf{f}_b$ , represents the two-way force per unit mass of the carrier flow due the dispersed bubbles, and  $\mathbf{u}$  is the local fluid velocity. The results show that  $DR_1$  dominates  $DR_2$  and increases with increasing  $We$ . The reason is that when the bubbles are more deformable, they are stretched along the streamwise direction similar to that of sub-Kolmogorov deformable bubbles (cf. section 2.1.2). The stretching reduces the projected surface area in the direction of the relative velocity which in turn lowers the bubble Reynolds number, leading to smaller wake, lower TKE, thus smaller  $\langle \varepsilon_B \rangle$  and lower  $DR_1$ .

### 3. DNS OF DROPLET-LADEN TURBULENT FLOWS

#### 3.1. Droplets of size smaller than the Kolmogorov length scale, $d < \eta$

Examples of liquid droplets of diameter  $d < \eta$  include rain droplets in the atmospheric boundary layer and fuel droplets in the combustion chambers of modern aircraft jet engines. Carl et al. (2001) measured the size distribution of the liquid fuel droplets under realistic conditions in the combustion chamber of an aircraft jet engine and their data show that the diameter of most droplets is smaller than  $\eta$  in the region downstream of the initial ligament breakup zone.

**3.1.1. Nondeformable droplets with  $d < \eta$ .** Mashayek (1998) performed DNS with the point-particle approach and  $96^3$  grid points to study droplet-turbulence interactions in a homogeneous shear flow. He considered both one-way and two-way couplings for non-evaporating and evaporating droplets. The number of droplets was  $1.5 \times 10^5$  and the diameter of non-evaporating droplets varied between  $0.2\eta$  and  $0.3\eta$ . The study showed that in the case of non-evaporating droplets, the turbulence kinetic energy is reduced and the flow anisotropy is increased due to the two-way coupling. In the case of evaporating droplets he found that the turbulence kinetic energy and the mean internal energy of the carrier flow are increased due the mass transfer of the droplet vapor to the carrier fluid.

Chen et al. (1998) studied the collision and coalescence of mono-sized droplets in a turbulent channel using DNS with the point particle approach at a friction Reynolds number,  $Re_\tau = 116$ . The droplet diameter ranged from  $0.1\eta$  to  $0.5\eta$  and the initial volume fraction was in the range  $5.8 \times 10^{-6} \leq \Phi_v \leq 3.1 \times 10^{-4}$ . The ratio of the liquid density to that of the carrier fluid varied from 20 to 2000. The results showed that the droplet inertia was the dominant factor in the collision mechanism. The results also showed that the predicted collision rate agreed with the theory of Saffman & Turner (1956) for droplets with response time in wall units  $\tau_d^+ < 1$ .

Miller & Bellan (1999) performed DNS of a confined temporally-developing mixing layer with one layer laden with evaporating liquid droplets using the point particle approach

and two-way coupling for mass, momentum and energy exchanges. The confining walls were treated as *frictionless and adiabatic* for simplifying the boundary conditions for the droplets and ensuring the conservation of mass and energy. The initial volume fraction of the droplets in the laden stream was  $5.5 \times 10^{-4}$ . The initial number of the mono-size droplets in the different cases varied from  $4 \times 10^4$  to  $7.3 \times 10^5$  and their initial diameter ranged from  $115\mu\text{m}$  to  $231\mu\text{m}$ . The Reynolds number based on the vorticity thickness was 200, and the convective Mach number  $M_c$  was 0.5. The initial temperatures of the gas and droplets were respectively  $350\text{K}$  and  $325\text{K}$ . The results show that the turbulence kinetic energy and the growth rate of the mixing layer were both attenuated monotonically by increasing the mass loading ratios of the droplets.

Leclercq & Bellan (2005) extended the mathematical formulation of Miller & Bellan (1999) to account for multi-component chemical composition of the liquid droplets. They examined the effects of the liquid composition on the development of the vortical features of the flow, the vortical state reached after the second pairing, and the gas temperature and composition. They concluded that the mixing layer growth and main rotational characteristics are unaffected by liquid specificity; however, the global mixing is highly liquid-specific. The analysis of the vorticity budgets showed that the small-scale vortical activity increases with increased fuel volatility.

Russo et al. (2014) studied the evaporation and condensation of water droplets in a turbulent channel flow in zero gravity at  $Re_\tau = 150$  using DNS with the point particle approach and two-way coupling of mass, momentum and heat between the two phases. The carrier fluid consisted of air and water vapor. One of the channel walls was heated while the other was cooled. This created a temperature gradient in the wall-normal direction and also a non-uniform mean vapor mass fraction. The objective of the study was to analyze the effects of phase change on the global heat transfer properties of the flow and on droplet motion and size distribution. Both the densities of the air and water vapor were time- and space-dependent, but their sum remained invariant to satisfy the zero divergence condition for the whole flow. The details of the pseudo-spectral numerical method are given in Kuerten (2006). The results show that initially the droplets migrate towards the channel walls due to turbophoresis (Reeks (1983)), thus increasing the droplet concentration in the vicinity of the walls. Simultaneously, evaporation and condensation result in the droplets growth near the cold wall and diminution near the warm wall. This also creates a gradient in water vapor concentration, directed from the cold to the warm wall. After reaching a steady state, the droplet concentration and mean droplet size become nearly constant. Turbulent diffusion of water vapor generates a mean flux of water vapor from the warm to the cold wall. Consequently, conservation of water mass results in a net mass flux of the droplets from the cold to the warm wall.

The results show that at steady state : (1) The heat transfer between the two walls for the droplet-laden flow, quantified by the Nusselt number, is larger by a factor of 3.5 than that of the single-phase flow, and by a factor of 2.6 than that of a flow laden with solid spherical particles having the same diameter, response time,  $\tau_p^+ = \tau_p u_\tau^2 / \nu$ , and specific heat of the droplets. This augmentation of heat transfer (by droplets vs. solid particles) is due to the latent heat of vaporization which reduces the droplet temperature near the hot wall and the latent heat of condensation which increases the droplet temperature near the cold wall. (2) The turbulence modulation of the carrier fluid by the droplets is the same as the modulation by solid particles. The Reynolds shear stresses and the TKE production are reduced in the wall region by the droplets. This finding is in contrast to that of Mashayek (1998) who found

that droplets evaporation enhanced the TKE production. In the simulation of Russo et al. (2014) both evaporation and condensation occur due to the presence of the hot and cold walls resulting in negligible net evaporation rate. The mean droplet diameter was found to be smaller near the warm wall than near the cold wall. It is noted that nucleation of droplets and droplet breakup were not accounted for in this study.

Kuerten & Vreman (2015) extended the DNS study of Russo et al. (2014) to include the effects of droplet collisions. The prescribed Weber number of the droplets was small such that coalescence between colliding droplets was negligible. The droplets overall volume fraction was in the range  $0.55 \times 10^{-4} \leq \Phi_{vo} \leq 2.2 \times 10^{-4}$ , and the corresponding number of droplets varied from  $0.5 \times 10^6$  to  $2 \times 10^6$ . The results show that droplet collisions (i.e. four-way coupling) cause a significant reduction (about 76%) of the maximum local concentrations of the droplets near the channel walls as compared to the two-way coupling case with the same overall  $\Phi_{vo}$ . Regarding the dependence of droplet collisions on  $\Phi_{vo}$ , Kuerten & Vreman (2015) stated that: “Elghobashi’s diagram (Elghobashi (1994)) indicates that the demarcation line between the two-way and four-way coupling regimes shifts toward lower volume fraction if the Stokes number becomes higher. However, in the present work, the Stokes number is only 10 in wall units, which shows that the effect of collisions on concentration in dilute flows is not limited to very high Stokes numbers.”

Two comments related to the above statement are made here to clarify the diagram of Elghobashi (1994): (i) The logarithmic-scale ordinate in the diagram is the Stokes number,  $St = \tau_p/\tau_K$ . The diagram shows that the demarcation line between the two-way and four-way regimes shifts toward lower volume fraction ( $< 10^{-3}$ ) for  $\tau_p/\tau_K \geq 0.7$  since the maximum preferential accumulation of solid particles in isotropic turbulence occurs at  $\tau_p/\tau_K = 1$  (Ferrante & Elghobashi (2003)). In other words, particle collisions are expected to start before the local concentration reaches its peak. (ii) If preferential accumulation occurs in a particle-laden turbulent flow, then the abscissa of the diagram should represent the *local volume fraction*,  $\phi_v$  (instead of the *overall volume fraction*,  $\Phi_{vo}$ ), to determine whether the regime *at a selected location* is two-way or four-way coupling.

The heat transfer results of Kuerten & Vreman (2015) indicate that accounting for the droplet collisions (four-way coupling) reduces Nusselt number by approximately 17% as compared to two-way coupling for the case with highest  $\Phi_{vo}$ . This means that a reduction of 76% in the maximum  $\phi_v$  near the wall resulted in *only* 17% reduction in Nusselt number. In order to explain this result we should note here that the large increase in Nusselt number when inertial particles are present in the flow is caused *totally* by the direct convective heat transfer between the particles and the carrier fluid due to their temperature difference. The reason for this *direct causality* is that the two-way momentum coupling between the particles and fluid *reduces* the turbulent shear stresses and TKE and hence *reduces* the turbulent heat fluxes within the carrier fluid, e.g. quantities proportional to  $\langle u_i T_f \rangle$ , where  $u_i$  and  $T_f$  are the fluctuations of the local fluid velocity and temperature (see Eqs. (20) and (21) in Kuerten & Vreman (2015)).

Now, the 76% reduction in the maximum  $\phi_v$  near the hot wall reduces the total surface area of the droplets across which heat is transferred from the hot fluid. Consequently, the fluid temperature (as well as the temperature difference between the fluid and droplets) near the hot wall is higher for the colliding droplets than in the case of no collisions. Thus, the Nusselt number reduction for the four-way coupling case is not as severe as that of  $\phi_v$ .



**3.1.2. Deformable droplets with  $d < \eta$ .** Cristini et al. (2003) studied the deformation and breakup of sub-Kolmogorov droplets in stationary isotropic turbulence. The objective was to enhance the understanding of the droplet breakup process beyond the phenomenological models of Kolmogorov (1949) and Hinze (1955). At the scale of these droplets, the viscous stresses,  $\mathcal{T}_\mu = (\mu/\tau_K)$ , dominate the inertial stresses,  $\mathcal{T}_\rho = (\rho d^2/\tau_K^2)$ , since  $\mathcal{T}_\mu/\mathcal{T}_\rho = \eta^2/d^2$ . Consequently, the local velocity field in the vicinity of these droplets was assumed to be governed by the Stokes flow equations. Both the viscosity ratio of the droplet fluid to the carrier fluid and the corresponding density ratio were set equal to unity (neutrally buoyant droplets). The droplets were treated as passive tracers with no effects on the carrier fluid. Under these conditions, it was assumed that the trajectory of a droplet center of mass is identical to that of the carrier fluid particle that coincided with it at an initial time. The velocity field of the stationary isotropic turbulence, at  $Re_\lambda = 54$ , was obtained using a pseudo-spectral DNS method.

The velocity field around a droplet was obtained by iteratively solving, at each time step, the boundary-integral equation for the Stokes flow on a set of interfacial marker points that were distributed on the surface of the initially spherical droplet. That velocity field is matched with the velocity of the turbulent flow near the droplet location via linear expansion. The boundary conditions for the local Stokes flow velocity field around the *deformable droplets* were prescribed at the droplet interface by the continuous velocity and tangential stress and the discontinuous normal stress due to surface tension. The droplet interface was adaptively restructured, between time steps, to maintain uniform resolution of the pointwise curvature with a prescribed accuracy as described in detail by Cristini et al. (2001). The results of Cristini et al. (2003) included the history of the deformation of two initially spherical droplets along their trajectories. Depending on the local shear/strain rates, the droplet deformation stages included stretched ellipsoids and dumbbells that led to neck thinning and pinch-off.

Biferale et al. (2014) studied the deformation and orientation statistics of sub-Kolmogorov ellipsoidal droplets in isotropic turbulence. Both the viscosity ratio of the droplet fluid to the carrier fluid and the corresponding density ratio were set equal to unity (neutrally buoyant droplets). The droplets were treated as passive tracers with no effects on the carrier fluid. Each of the simulated droplets followed the trajectory of the carrier fluid particle coinciding with its center at an initial time. The stationary homogeneous isotropic turbulent flow was computed via DNS at  $Re_\lambda = 185$  and 400. The ellipsoidal droplet shape evolution was predicted via the phenomenological equation of Maffettone & Minale (1998) described earlier in section 2.1.2. The prescribed initial droplet size was such that  $d/\eta \leq 0.1$ . The trajectories of  $7 \times 10^3$  droplets for the  $Re_\lambda = 185$  case and  $15 \times 10^3$  droplets for the  $Re_\lambda = 400$  case were computed. The results show, as expected, that increasing the Capillary number,  $Ca$ , for a given  $\tau_K$ , the droplet deformation increases. The deformation of a typical droplet may follow a sequence of oblate, prolate and then return to spherical shape. A critical Capillary number was identified at which the droplet elongation along one or two directions becomes unbounded, which should eventually lead to droplet breakup.

Spandan et al. (2016) studied the deformation and orientation statistics of neutrally buoyant sub-Kolmogorov ellipsoidal droplets in turbulent Taylor-Couette flow. They followed the same approach of Biferale et al. (2014), and their own study of the sub-Kolmogorov bubbles (Spandan et al. (2017b)) described above in section 2.1.2.

Spandan et al. (2016) named the approach of considering the droplet as a massless passive tracer a *zero-way coupling*. However, *zero-way coupling* means *no coupling*, and certainly

this is not the case of a tracer following the identical instantaneous Lagrangian motion of a fluid particle. A *tracer* or *passive scalar* is a more appropriate name for this approach.

The droplet sizes were in the range of  $0.05 \leq d/\eta \leq 0.15$  even during the deformation. The DNS were performed for two inner cylinder Reynolds numbers ( $Re_i = 2500, 5000$ ), four different Capillary numbers ( $Ca = \tau/\tau_K = (\eta\mu_f)/(\sigma\tau_K) = 0.05, 0.1, 0.2$  and  $0.3$ ), and two viscosity ratios ( $\hat{\mu} = 1$  and  $100$ ).

The statistical analysis of the droplet deformation was performed using the dimensionless *deformation parameter*  $D$  defined above in section 2.1.2. The results show that the maximum values of  $D$  occur near both the rotating and stationary walls, and as expected,  $D$  increases with increasing the Capillary number,  $Ca$ . However, the peak of the  $D$  profile moves away from the wall with increasing  $Ca$ . This is a result of the elastic collision model used for the interaction of the droplet with the wall. The center of mass of a highly stretched droplet is displaced away from the wall as compared to that of a less deformed droplet.

### 3.2. Droplets of size larger than the Kolmogorov length scale, $d > \eta$

#### 3.2.1. Single droplet deformation and evaporation in isotropic turbulence using LBM.

Albernaz et al. (2017) used a *hybrid* lattice Boltzmann method (LBM) to study the deformation and evaporation of a single droplet in stationary isotropic turbulence. In their hybrid method, the fluid density and velocity fields were obtained via LBM with D3Q19 lattice and multirelaxation-time (MRT) collision operator (d’Humières et al. (2002)), but the internal energy conservation equation was solved by the finite-difference scheme of Lallemand & Luo (2003). In the D3Q19 lattice, “D3” denotes three-dimensional flow and the “Q” refers to the first author of the paper Qian et al. (1992). The number 19 indicates that a fluid point at the center of the cubic lattice interacts with the 18 neighboring points (=12 points of intersection of the three midplanes with the edges of the cube + 6 points of intersection of the three midplanes at the six surfaces of the cube). A fluid point at the center of the cube has 18 possible velocity directions plus a zero velocity. The internal energy equation contained a correction term proportional to the difference between the mean pressure of the domain and the initial reference pressure. The correction is needed for conditions close to the critical point where fluctuations of thermodynamic properties occur. Forcing at low wavenumbers using the method of Kareem et al. (2009) was applied at every time step to generate a statistically stationary velocity field for  $73 \leq Re_\lambda \leq 133$ .

The pseudo-potential method of Shan & Chen (1993) and Kupershtokh & Medvedev (2006) was used to simulate the droplet in the LBM. The liquid hexane droplet was surrounded by its vapor as the carrier fluid. The interface between the liquid and vapor was considered as a thin transition layer of finite width (several nodes of lattice) where the density changes smoothly from one phase to the other. The ratio of the liquid density to that of the vapor was  $\approx 10$ . Also, the ratio of the liquid dynamic viscosity to that of the vapor was  $\approx 10$ , since both liquid and vapor had identical kinematic viscosity. The surface tension,  $\sigma$ , was calculated via the Young-Laplace equation which relates the pressure jump across the interface to the product of  $\sigma$  and the local curvature (Landau & Lifshitz (1959)).

The initial temperature of both the liquid and vapor was prescribed equal to  $0.9T_{critical}$  of hexane. The initial droplet diameter,  $d_o$ , ranged from  $50\eta$  to  $80\eta$ , which corresponds to the range of  $2.4\lambda$  to  $3.8\lambda$ .

The effect of surface tension on the droplet deformation was studied by varying the Ohnesorge number,  $Oh = \mu_\ell/\sqrt{\rho_\ell\sigma d} = \sqrt{We_\ell}/Re_\ell$ , in the range  $4.2 \times 10^{-3} \leq Oh \leq 6 \times 10^{-3}$ ,



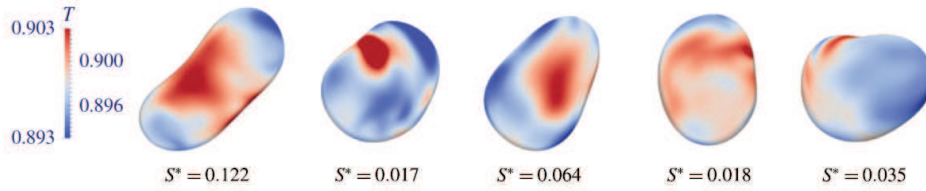


**Figure 4**

Temperature distribution over the droplet surface for different values of the deformation parameter  $S^* = (S - S_0)/S_0$ , where  $S$  is the instantaneous area of the droplet surface, and  $S_0$  is the equivalent surface area of a sphere whose volume is identical to that of the deformed droplet. Source: [Albernaz et al. \(2017\)](#) with permission from Cambridge Univ. Press.

where  $\mu_\ell$  and  $\rho_\ell$  are the dynamic viscosity and density of the droplet. Some interesting results of this study are:

- For a fixed  $Re_\lambda$ , increasing  $d_o$  increases the kinetic energy of the carrier fluid and reduces the kinetic energy of the droplet since the total kinetic energy is a function of the fixed  $Re_\lambda$ .
- The droplet deformation increases with increasing  $d_o$  due to the increase of Weber number.
- Reducing the surface tension increases the fluctuations of the thermodynamic properties, thus increasing the evaporation rate.
- At the droplet surface, low temperature regions are associated with stronger curvature whereas higher temperature occurs in flatter surface regions (Fig.4).
- Droplet volume fluctuations are correlated with vapor temperature fluctuations. Strong correlations occur between positive temperature fluctuations and vapor condensation.

### 3.2.2. Single droplet deformation in a turbulent channel flow using PFM.

[Scarbolo & Soldati \(2013\)](#) used the Phase Field Model (PFM), section 1, of [Gurtin et al. \(1996\)](#) to study the deformation of a single droplet released in a fully developed turbulent channel flow at  $Re_\tau = 100$ . The ratios of the liquid density and viscosity of the droplet to those of the carrier fluid were prescribed equal to unity. As described earlier in section 1, the forcing term representing the surface tension effects was added to the NS equations. The modified NS equations were solved together with the phase field transport equation of [Cahn & Hilliard \(1959\)](#). The initial droplet diameter was  $d_o = 0.8H$ , where  $H$  is half the channel height, and  $7.7 \leq d_o/\eta \leq 16.7$ . The Weber number,  $We = (\rho u_\tau^2 H)/\sigma$ , was in the range  $5.3 \times 10^{-3} \leq We \leq 42.4 \times 10^{-3}$ . For that range of  $We$ , the mass loss at the end of the simulation varied from 4% to 14%. The results show that the TKE reaches its minimum value at the interface. The vorticity peak occurs at a distance of  $\sim d/4$  from the droplet interface, and the magnitude of that peak decreases with decreasing  $We$  (see Fig. 5 in [Scarbolo & Soldati \(2013\)](#)).

[Scarbolo et al. \(2013\)](#) compared the performance of PFM with that of LBM (described in subsection 3.2.1 above) in simulating the deformation of a single 2D cylindrical droplet in simple shear flows. The comparison showed that the PFM's computational cost is almost three times higher than that of LBM. However, the results of the PFM appear to be more

accurate in that the spurious currents of the local kinetic energy created along the droplet interface were smaller in PFM than in LBM by two orders of magnitude (see Fig.1 in Scarbolo et al. (2013)).

### 3.2.3. Coalescence and breakup of large droplets in turbulent channel flow using PFM.

Scarbolo et al. (2015) used the above described PFM in simulating droplets with initial number  $N_0 = 256$ , and volume fraction  $\Phi_v = 0.054$ , in a DNS of a fully developed turbulent channel flow at  $Re_\tau = 150$ . The objective was to study the interactions between the droplets. The ratios of the liquid density and viscosity of the droplet to those of the carrier fluid were prescribed equal to unity. The initial droplet diameter  $d_o = 0.4H$ , and  $15.9 \leq d_o/\eta \leq 37$ , where  $H$  is half the channel height. The interface thickness,  $\xi$ , was a constant prescribed via Cahn number,  $Ch = \xi/H = 0.0185$ , which resulted in  $0.36 \leq \eta/Ch \leq 0.84$ , thus minimizing the effects of the smallest eddies on distorting the interface. The mass loss at the end of the simulation varied from 2% to 10% for the range of  $0.18 \leq We \leq 2.8$ . The results show that droplets, under the selected conditions and fluid properties, migrate away from the wall toward the channel center. The study identified two regimes of droplets interactions based on the Weber number. For  $We < 1$ , the relatively large surface tension prevents droplet breakup, and allows coalescence events to prevail. Eventually, for  $t^+ > 2000$  (in wall units), the number of the merged droplets becomes  $< N_0$ , and their separation distances increase resulting in diminished collisions.

In contrast, for  $We > 1$ , the droplets breakup and coalescence processes occur simultaneously during an early transition period. This is followed at large  $t^+$  by a dynamic equilibrium state at which the number of droplets reaches an asymptotic value which is about an order of magnitude larger than that for the case of  $We < 1$ .

Scarbolo et al. (2016) performed DNS with the same flow conditions and fluid properties of the above described study of Scarbolo et al. (2015) to investigate turbulence modification by dispersed deformable droplets. The results show that for  $We > 1$  the normalized wall shear stress or friction coefficient,  $C_f$ , for the channel flow is not affected by the deformed droplets and its temporal development is nearly the same as that of the single-phase flow. However, for  $We < 1$ , the temporal development of  $C_f$  shows a gradual increase at early times, reaching a peak at  $1000 \leq t^+ \leq 2000$ , followed by a gradual reduction. The physical explanation for these observations was not provided.

Roccon et al. (2017) extended the DNS study of Scarbolo et al. (2016), described above, by relaxing the restriction of unity viscosity ratio to examine the effects of varying the viscosity of the droplet. Five different values of the dynamic viscosity ratio,  $\hat{\mu} = 0.01, 0.1, 1, 10, 100$ , and three values of Weber number,  $We = 0.75, 1.5, 3$ , were studied providing a total of 15 test cases.

The initial number of droplets was  $N_0 = 256$ , at a volume fraction  $\Phi_{vo} = 0.183$  and initial droplet diameter  $= 0.6H$ .

The results show that for all test cases, the deformable droplets migrate away from the wall and reduce the wall friction slightly as indicated by an increase of the average mean velocity in the central zone of the channel by  $\sim 2\% - 4\%$ .

Qualitatively, the results show, as expected, that increasing the droplet viscosity or surface tension decreases the breakup rate. For the case of the highest surface tension,  $We = 0.75$ , droplets coalescence rate overtakes their breakup rate for all values of  $\hat{\mu}$ , resulting in a gradual reduction of the number of droplets (Fig.5) which reaches after time  $t^+ = 1000$  an asymptotic value of about  $0.04N_0$ . For the lowest surface tension,  $We = 3$ , the effect of

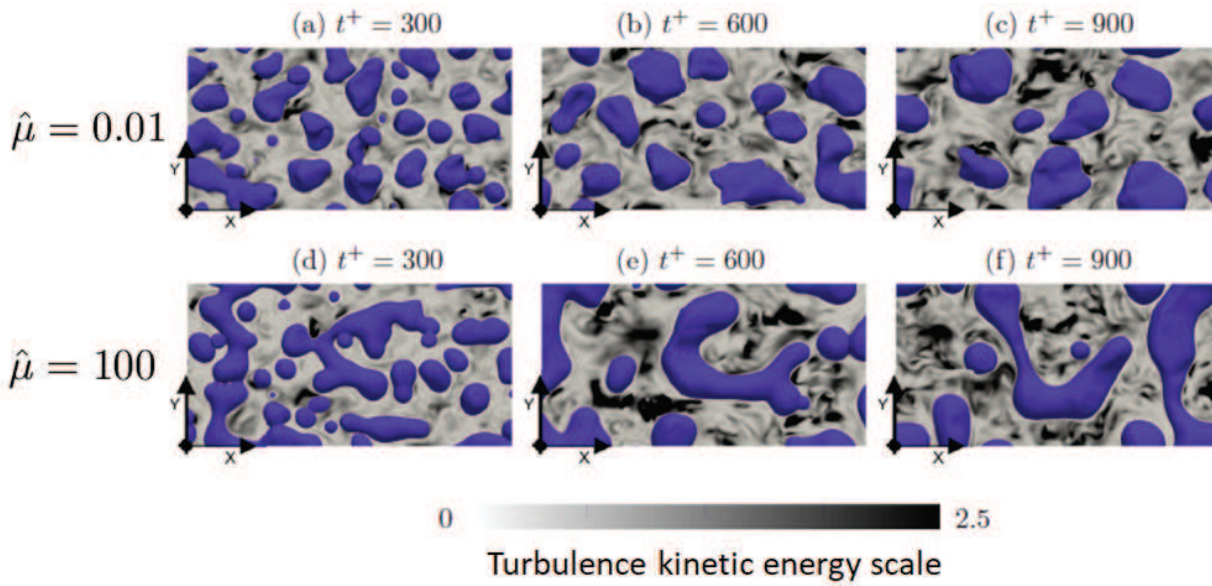


**Figure 5**

Temporal evolution of droplets for  $We = 0.75$  and for two viscosity ratios (a-c)  $\hat{\mu} = 0.01$  and (d-f)  $\hat{\mu} = 100$ . Each panel refers to a given time instant ( $t^+ = 300, 600$ , and  $900$ ). Iso-contours of TKE computed on a plane passing through the channel center are shown in grey scale. Source: Roccon et al. (2017) with permission from The American Physical society.

varying  $\hat{\mu}$  becomes more pronounced (Fig.6). For  $\hat{\mu} \leq 1$ , the breakup rate increases and the asymptotic value of droplets number is about  $0.4N_0$ . For  $\hat{\mu} = 10$ , the breakup rate decreases and the droplets number reaches  $0.1N_0$ . For  $\hat{\mu} = 100$ , the coalescence rate prevails and the droplets number diminishes to  $0.01N_0$ .

These results show that lowering the droplet viscosity (relative to that of the carrier fluid), at a fixed surface tension, enhances the droplet deformation and the eventual breakup. The results also show, as expected, that the mean curvature of the interface between the droplet and the carrier fluid depends on  $\hat{\mu}$ . The interface is defined as the isosurface of the scalar phase field function  $\phi(\mathbf{x}, t) = 0$ , and its mean curvature is  $\kappa = \nabla \cdot \left( -\frac{\nabla \phi}{|\nabla \phi|} \right)$  (Sun & Beckermann (2007)). The case of lowest surface tension,  $We = 3$ , and smallest  $\hat{\mu} = 0.01$  resulted in strong curvature and breakup leading to the creation of small droplets (Fig.6). In contrast, for the same surface tension and  $\hat{\mu} = 100$ , large elongated droplets with relatively small curvatures were created (Fig.6).

### 3.2.4. Dispersion of liquid droplets in isotropic turbulence using LBM-PFM.

Komrakova et al. (2015) used the *free-energy* LBM of Swift et al. (1996) in which the diffuse interface evolves naturally according to thermodynamics. This *free-energy* LBM is a hybrid of LBM and PFM. Two probability density functions,  $f_i^n(\mathbf{x}, t)$ ,  $n = 2$ , described earlier in section 1 are used: one to solve the continuity and NS equations for the carrier fluid, and the other to solve the Cahn-Hilliard equation (Cahn & Hilliard (1959)) described in section 1. A single relaxation time collision operator (Bhatnagar et al. (1954)) was used in the solution.

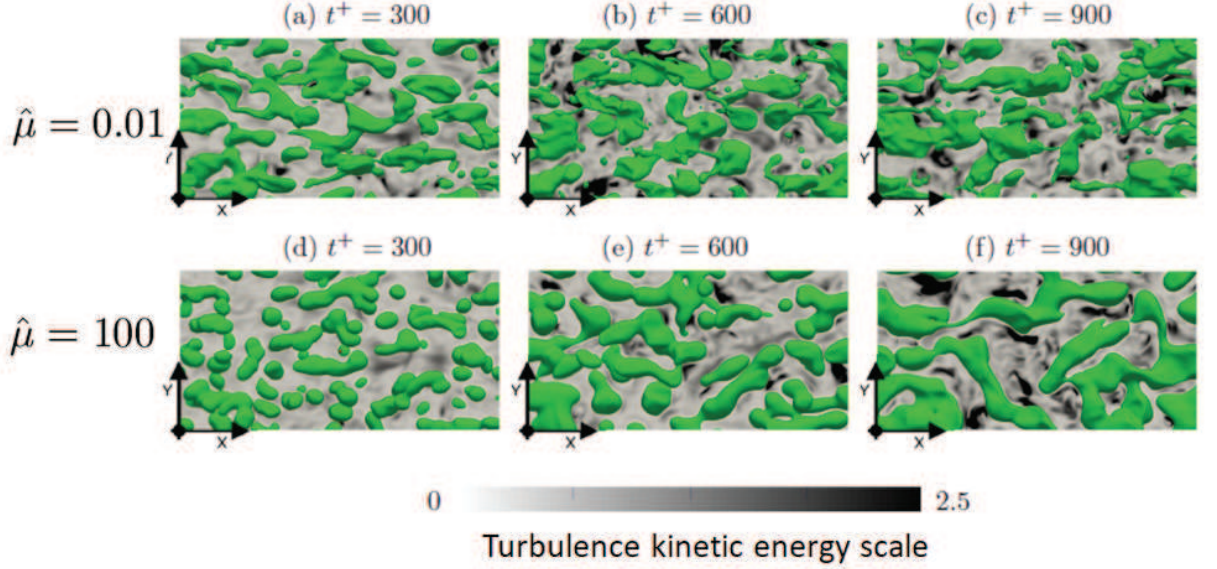


**Figure 6**

Temporal evolution of droplets for  $We = 3$  and for two viscosity ratios (a-c)  $\hat{\mu} = 0.01$  and (d-f)  $\hat{\mu} = 100$ . Each panel refers to a given time instant ( $t^+ = 300, 600$ , and  $900$ ). Iso-contours of TKE computed on a plane passing through the channel center are shown in grey scale. Source: [Roccon et al. \(2017\)](#) with permission from The American Physical society.

The D3Q19 lattice (section 3.2.1) was used to perform DNS of stationary isotropic turbulence generated by the linear forcing method of [Lundgren \(2003\)](#). The periodic cubic computational domain contained a maximum of  $1000^3$  dimensionless *lattice units* [lu] where the Kolmogorov length scale  $\eta \sim 1-10$  [lu]. The Reynolds number  $Re_\lambda$  could not be prescribed as an input parameter since the velocity  $u_{rms}$  is not known a priori. Only three parameters were used to prescribe the turbulent two-phase flow: the droplets volume fraction,  $\Phi_{vo}$ , the viscosity ratio,  $\hat{\mu}$ , and the Capillary number,  $Ca = \tau/\tau_K = (\eta\mu_f)/(\sigma\tau_K)$ , where  $\mu_f$  is the dynamic viscosity of the carrier fluid. The density ratio of the droplet to that of the carrier fluid was set to unity, and the viscosity ratio was  $0.3 \leq \hat{\mu} \leq 1$ .

The DNS starts at  $t = 0$  with a single droplet placed in the computational domain with a volume fraction range  $0.001 \leq \Phi_{vo} \leq 0.2$ . The initial droplet diameter was in the range of  $20\eta-30\eta$ . The droplet breaks up due to the turbulent stresses in the carrier fluid as shown in Fig.7. The Reynolds number was computed from the DNS results for the case shown in Fig.7 as  $Re_\lambda = 42$  ([Komrakova \(2017\)](#)). The study points out to the following limitations of the DNS using LBM-PFM: (a) Coalescence occurs when the interfaces of multiple droplets occupy the same computational cell. Thus, in order to suppress unphysical coalescence, it is necessary to resolve the liquid film between the droplets which requires prohibitive mesh refinement ([Shardt et al. \(2013\)](#)). (b) Dissolution of small droplets is an inherent property of the numerical method ([Keestra et al. \(2003\)](#)). The dissolution rate increases as the droplet size decreases. To minimize the dissolution, it is necessary to increase the resolution by keeping the droplet diameter in the range of  $20\eta-30\eta$ . (c) It is not possible to obtain



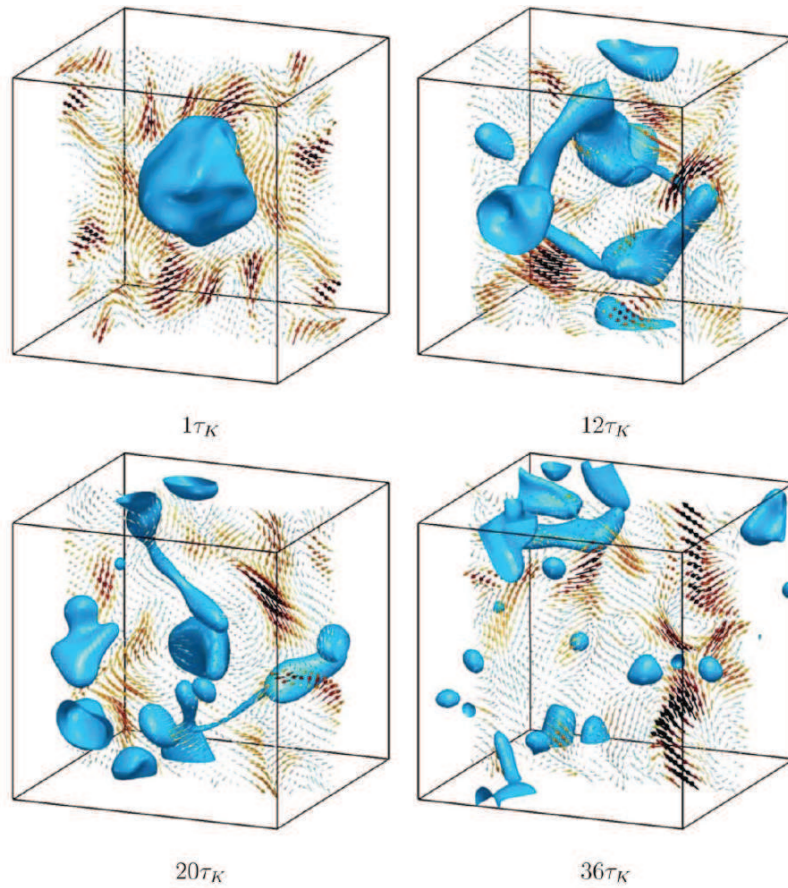


**Figure 7**

Iso-surfaces of the scalar phase field  $\phi = 0$  representing the surface of the dispersed liquid droplet and velocity vectors at different time instants relative to the Kolmogorov time scale,  $\tau_K$ , for the case with  $\eta = 1$  [Lattice Unit], viscosity ratio  $\hat{\mu} = 1$ , density ratio = 1, and the Capillary number  $Ca = 0.1$ . The dispersed phase volume fraction is  $\Phi_v = 0.03$ . The initial single droplet is placed in the isotropic turbulence at  $t = 0$ . Source: Komrakova et al. (2015) with permission from AIChE.

an accurate TKE spectrum of a two-phase turbulent flow. It is known that LBM is prone to generation of spurious currents due to discretization of the velocity space. The order of magnitude of the spurious currents can be the same as that of the actual velocity field. In addition, the spurious currents appear within the diffuse interface and interact with the small scale motion leading to a significant unphysical energy gain at high wavenumbers.

**3.2.5. The interaction between 3130 fully resolved droplets and isotropic turbulence using VOF.** Dodd & Ferrante (2016) performed DNS of decaying isotropic turbulence, with an initial  $Re_\lambda = 83$ , laden with 3130 nonvaporizing droplets with  $d \approx 20\eta \approx \lambda$ . The ranges of the density and dynamic viscosity ratios were  $1 \leq \hat{\rho} \leq 100$  and  $1 \leq \hat{\mu} \leq 100$ , respectively. The Weber number based on the r.m.s. velocity of the carrier fluid was in the range

$0.1 \leq We_{rms} \leq 5$ . The volume fraction of the droplets was  $\Phi_v = 0.05$  and the mass fraction ranged from 0.5 to 5.

Before discussing the results of the simulations, it is worth describing the novel method developed by [Dodd & Ferrante \(2016\)](#) for solving the Poisson equation for the pressure in an incompressible immiscible two-fluid flows *with large density and dynamic viscosity ratios*. The method is described in detail by [Dodd & Ferrante \(2014\)](#). It is well known that the numerical solution of NS equations of two-fluid flows with nonuniform density requires solving a *variable-coefficient* Poisson equation for the pressure in the form

$$\nabla \cdot \left( \frac{1}{\rho^{n+1}} \nabla p^{n+1} \right) = \frac{1}{\Delta t} \nabla \cdot \mathbf{u}^*, \quad (10)$$

where  $\mathbf{u}^*$  is the approximate fluid velocity at time step  $n + 1$ . Solution of (10) is conventionally performed using iterative multigrid methods ([Gueyffier et al. \(1999\)](#)) or multigrid-preconditioned Krylov methods ([Sussman & Puckett \(2000\)](#)). All these methods are much slower than the fast Poisson solvers (e.g. FFT). However, the latter require the coefficient of  $\nabla p^{n+1}$  to be a constant, whereas the coefficient  $\frac{1}{\rho^{n+1}}$  on the LHS of (10) varies in space and time. In order to overcome this problem, [Dong & Shen \(2012\)](#) split the product inside the brackets of (10) in a way to render the variable coefficient of  $\nabla p^{n+1}$  a constant. The first step is to approximate the the product on the LHS of (10) as

$$\left( \frac{1}{\rho^{n+1}} \nabla p^{n+1} \right) \approx \frac{1}{\rho_0} \nabla p^{n+1} + \left( \frac{1}{\rho^{n+1}} - \frac{1}{\rho_0} \right) \nabla p^*, \quad (11)$$

where  $\rho_0 = \min(\rho_1, \rho_2)$  and  $p^* = 2p^n - p^{n-1}$ . Then, substitution of the approximation (11) into (10) results in:

$$\nabla^2 p^{n+1} = \nabla \cdot \left[ \left( 1 - \frac{\rho_0}{\rho^{n+1}} \right) \nabla p^* \right] + \frac{\rho_0}{\Delta t} \nabla \cdot \mathbf{u}^*, \quad (12)$$

which can be solved using fast Poisson solvers. [Dodd & Ferrante \(2014\)](#) compared the accuracy and speed of solving (12) for several canonical two-phase flows, at density and dynamic viscosity ratios of values up to  $10^4$ , with that of (10) and concluded that the new split method is at least an order of magnitude faster than that of (10) for the same accuracy level.

Now, we continue the discussion of the main results of [Dodd & Ferrante \(2016\)](#), hereinafter referred to as DF. In order to explain the exchanges of TKE between the droplets and the carrier fluid, DF derived three TKE transport equations for the droplet phase, the carrier fluid and the combined two-fluid flow [see Eqs. (B19), (B20), (B21) and (C8) in [Dodd & Ferrante \(2016\)](#)]. For the first two equations, the TKE decay rate is governed by the sum of the viscous dissipation rate,  $-\varepsilon$ , the viscous power,  $T_\nu$ , and pressure power,  $T_p$ . For the combined two-fluid, the TKE decay rate equals the sum of the viscous dissipation rate and the power due to surface tension,  $\Psi_\sigma$ , which is the rate of work done by the surface tension forces on the fluid.  $\Psi_\sigma$  can be a source or sink of TKE, depending on whether the total surface area of droplets decreases (e.g., coalescence) or increases (e.g., breakup), respectively. Figure 8 shows a schematic of the TKE exchanges according to the three TKE transport equations. The subscripts  $c, d$  in the figure denote the carrier fluid and droplets respectively.

DF performed DNS for seven cases by varying  $We_{rms}$ , the density ratio,  $\hat{\rho}$  or the dynamic

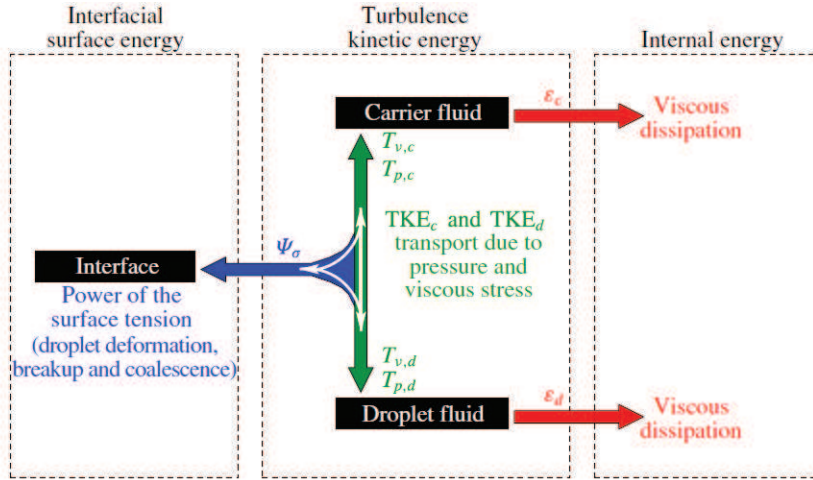


**Figure 8**

Schematic showing TKE exchanges between the droplets and carrier fluid turbulence. The three bounding rectangles from left to right represent the interactions between interfacial surface energy, TKE, and internal energy. The blue arrow represents the two-way exchange between TKE and interfacial surface energy by the power of the surface tension,  $\Psi_\sigma$ . The green arrows denote the transport of TKE between the two fluids while exchanging TKE for surface energy via  $\Psi_\sigma$ . The red arrows represent the transformation of TKE of the carrier fluid and droplet into internal energy by viscous dissipation. [ From Fig. 5 of [Dodd & Ferrante \(2016\)](#) with permission from Cambridge Univ. Press. ]

viscosity ratio,  $\hat{\mu}$ . Increasing  $W_{rms}$  from 0.1 in case B to 5 in case D showed that the number of droplets at the end of the simulation decreased relative to their initial number by about 20% due to coalescence in B, and increased by about 27% in D due to breakup. In case B, the power  $\Psi_\sigma$  due to coalescence represents a source of TKE equal to about 50% of the magnitude of the viscous dissipation rate.

Figure 9 compares the viscous dissipation rate for cases E and F where both have the same  $\hat{\mu} = 10$ , but their  $\hat{\rho} = 1$  and 100 respectively. The response time,  $\tau_d$ , of the denser F droplets is 100 times that of the E droplets. Thus the F droplets generate higher fluid strain rates near their surfaces than do the E droplets, and hence the dissipation rates are higher in F as shown in Figure 9.

#### 4. CONCLUDING REMARKS

1. Significant progress has been made during the past 20 years in DNS of turbulent flows laden with droplets or bubbles. This progress is due to the continuing development of the numerical methods discussed above and the advances in supercomputer hardware and software. However, due to the complexity of these flows the experimental data needed to validate the DNS results are virtually nonexistent. The needed experimental data should provide local instantaneous measurements of the velocity fields of

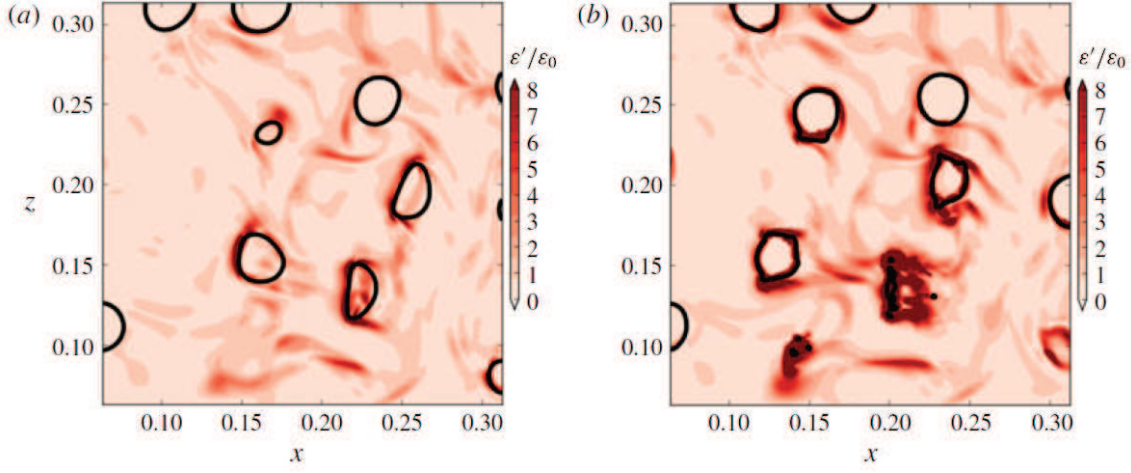


**Figure 9**

Comparison of the viscous dissipation rate of cases E in (a) and F in (b). Both cases have the same dynamic viscosity ratio  $\hat{\mu} = 10$ , but case E has a density ratio  $\hat{\rho} = 1$ , whereas case F has  $\hat{\rho} = 100$ . Source: Fig. 12 of [Dodd & Ferrante \(2016\)](#) with permission from Cambridge Univ. Press.

- both the carrier fluid and the dispersed phase in addition to instantaneous images of shape changes of the latter.
2. Since Large Eddy Simulation will be used for the foreseeable future to predict turbulent multiphase flows at practical Reynolds numbers, accurate subgrid scale (SGS) models need to be developed and validated by DNS results such as those described above. It is noted here that such accurate SGS models do not exist at present.
  3. The phenomenological equation of [Maffettone & Minale \(1998\)](#) provides a powerful tool for accounting of shape changes of deformable bubbles or droplets which are smaller than the Kolmogorov length scale,  $\eta$ .
  4. All the reviewed DNS studies of fully resolved droplets or bubbles, except that of [Dodd & Ferrante \(2016\)](#), restricted the density and viscosity ratios of the two interacting phases in the range of 1 to 10. Both the density and viscosity ratios were equal to  $10^2$  in the study of [Dodd & Ferrante \(2016\)](#). Furthermore, [Dodd & Ferrante \(2014\)](#) validated their numerical method with the analytical solution of the capillary wave of [Prosperetti \(1981\)](#) for density and viscosity ratios up to  $10^4$ , and with the experimental data of [Beard \(1976\)](#) for a falling droplet for a density ratio of  $10^3$ .
  5. The PFM provides qualitatively interesting results, however it suffers from the following drawbacks : (a) The large width of the interface region (4-8 cells) leads to errors in the curvature ([Jacqmin \(1999\)](#)). (b) The mass conservation is not satisfied ([Yue et al. \(2007\)](#)) as confirmed by [Scarbolo & Soldati \(2013\)](#) who showed that the mass loss at the end of the simulation varied from 4% to 14%, and from 2% to 10% in the study of [Scarbolo et al. \(2015\)](#). This inability to conserve mass renders the PFM quite inaccurate for cases involving vaporization or condensation as well as droplet motion in highly vortical flows.



## DISCLOSURE STATEMENT

The author is not aware of any affiliations, memberships, funding, or financial holdings that might be perceived as affecting the objectivity of this review.

## ACKNOWLEDGMENTS

The author thanks Professors William Sirignano, Andrea Prosperetti, Detlef Lohse, Alfredo Soldati and Antonino Ferrante for their helpful comments on the first draft of this article.

## LITERATURE CITED

- Albernaz DL, Do-Quang M, Hermanson JC, Amberg G. 2017. Droplet deformation and heat transfer in isotropic turbulence. *J. Fluid Mech.* 820:61–85
- Anderson DM, McFadden GB, Wheeler AA. 1998. Diffuse-interface methods in fluid mechanics. *Annu. Rev. Fluid Mech.* 30:139–165
- Auton T. 1987. The lift force on a spherical body in a rotational flow. *J. Fluid Mech.* 183:199–218
- Auton T, Hunt J, Prud'homme M. 1988. The force exerted on a body in inviscid unsteady non-uniform rotational flow. *J. Fluid Mech.* 197:241–257
- Balachandar S, Eaton J. 2010. Turbulent dispersed multiphase flow. *Annu. Rev. Fluid Mech.* 42:111–133
- Beard K. 1976. Terminal velocity and shape of cloud and precipitation drops aloft. *J. Atmos. Sci.* 33:851–864
- Bhatnagar PL, Gross EP, Krook M. 1954. A model for collision processes in gases. I. small amplitude processes in charged and neutral one-component systems. *Phys. Rev.* 94:511–525
- Biferale L, Meneveau C, Verzicco R. 2014. Deformation statistics of sub-Kolmogorov-scale ellipsoidal neutrally buoyant drops in isotropic turbulence. *J. Fluid Mech.* 754:184–207
- Cahn JW, Hilliard JE. 1959. Free energy of a nonuniform system. III. Nucleation in a two-component incompressible fluid. *J. Chem. Phys.* 31:688–699
- Carl M, Behrendt T, Fleing C, Frodermann M, Heinze J, et al. 2001. Experimental and numerical investigation of a planar combustor sector at realistic operating conditions. *J. Engineering for Gas Turbines and Power* 123:811–816
- Chen M, Kontomaris K, McLaughlin J. 1998. Direct numerical simulation of droplet collisions in a turbulent channel flow. part ii: collision rates. *Int. J. of Multiphase Flow* 24:1105–1138
- Cristini V, Blawdziewicz J, Loewenberg M. 2001. An adaptive mesh algorithm for evolving surfaces: Simulations of drop breakup and coalescence. *J. Comp. Physics* 168:445–463
- Cristini V, Blawdziewicz J, Loewenberg M, Collins L. 2003. Breakup in stochastic stokes flows: sub-kolmogorov drops in isotropic turbulence. *J. Fluid Mech.* 492:231–250
- Desjardins O, Moureau V, Pitsch H. 2008. An accurate conservative level set/ghost fluid method for simulating turbulent atomization. *J. Comp. Physics* 227:8395–8416
- deTullio M, Pascazio G. 2016. A moving-least-squares immersed boundary method for simulating the fluid-structure interaction of elastic bodies with arbitrary thickness. *J. Comp. Physics* 325:201–225
- d'Humières D, Ginzburg I, Krafczyk M, Lallemand P, Luo L. 2002. Lattice Boltzmann multiple-relaxation-time models in three dimensions. *Proc. R. Soc. London A* 360:427–451
- Dodd M, Ferrante A. 2014. A fast pressure-correction method for incompressible two-fluid flows. *J. Comp. Physics* 273:416–434
- Dodd M, Ferrante A. 2016. On the interaction of Taylor length scale size droplets and isotropic turbulence. *J. Fluid Mech.* 806:356–412
- Dong S, Shen J. 2012. A time-stepping scheme involving constant coefficient matrices for phase-

- field simulations of two-phase incompressible flows with large density ratios. *J. Comp. Physics* 231:5788–5804
- Druzhinin O, Elghobashi S. 1998. Direct numerical simulations of bubble-laden turbulent flows using the two-fluid formulation. *Phys. Fluids* 10:685–697
- Druzhinin O, Elghobashi S. 2001. Direct numerical simulation of a spatially-developing three-dimensional bubble-laden mixing layer with two-way coupling. *J. Fluid Mech.* 429:23–61
- Elghobashi S. 1994. On predicting particle-laden turbulent flows. *Appl. Sci. Res.* 52:309–329
- Elghobashi S, Prosperetti A. 2009. Preface. *Int. J. Multiphase Flow* 35:791
- Elghobashi S, Truesdell G. 1993. On the two-way interaction between homogeneous turbulence and dispersed solid particles, part 1 : turbulence modification. *Phys. Fluids* A5:1790–1801
- Ferrante A, Elghobashi S. 2003. On the physical mechanisms of two-way coupling in particle-laden isotropic turbulence. *Phys. Fluids* 15:315–329
- Ferrante A, Elghobashi S. 2004. On the physical mechanisms of drag reduction in a spatially-developing turbulent boundary layer laden with microbubbles. *J. Fluid Mech.* 503:345–355
- Ferrante A, Elghobashi S. 2007. On the effects of microbubbles on the Taylor-Green vortex flow. *J. Fluid Mech.* 572:145–177
- Gueyffier D, Li J, Nadim A, Scardovelli R, Zaleski S. 1999. Volume-of-fluid interface tracking with smoothed surface stress methods for three-dimensional flows. *J. Comp. Physics* 152:423–456
- Guido S, Minale M, Maffettone P. 2000. Drop shape dynamics under shear-flow reversal. *J. Rheology* 44:1385–1399
- Gurtin M, Fried E, Anand L. 2010. The mechanics and thermodynamics of continua. Cambridge university Press
- Gurtin ME, Polignone D, Vinals J. 1996. Two-phase binary fluids and immiscible fluids described by an order parameter. *Math. Models and Methods in Appl. Sci.* 6:815–831
- Hinze J. 1955. Fundamentals of the hydrodynamic mechanism of splitting in dispersion processes. *AICHE J.* 1:289–295
- Jacqmin D. 1999. Calculation of two-phase Navier-Stokes flows using phase-field modeling. *J. Comp. Physics* 155:96–127
- Kareem WA, Izawa S, Xiong AK, Fukunishi Y. 2009. Lattice Boltzmann simulations of homogeneous isotropic turbulence. *Comput. Maths Applics.* 58:10551061
- Keestra B, Van Puyvelde P, Anderson P, Meijer HEH. 2003. Diffuse interface modeling of the morphology and rheology of immiscible polymer blends. *Phys. Fluids* 15:2567–2575
- Kolmogorov A. 1949. On the disintegration of drops in turbulent flow. *Dokl. Akad. Nauk.* 66:825–828
- Komrakova AE. 2017. *Private Communication*
- Komrakova AE, Eskin D, Derksen JJ. 2015. Numerical study of turbulent liquid-liquid dispersions. *AICHE J.* 61:2618–2633
- Kuerten J. 2006. Subgrid modeling in particle-laden channel flow. *Phys. Fluids* 18:025108–1–13
- Kuerten J, Vreman A. 2015. Effect of droplet interaction on droplet-laden turbulent channel flow. *Phys. Fluids* 27:053304–1–22
- Kupershtokh A, Medvedev D. 2006. Lattice Boltzmann equation method in electrohydrodynamic problems. *Journal of Electrostatics* 64:581–585
- Lallemand P, Luo LS. 2003. Hybrid finite-difference thermal lattice Boltzmann equation. *Int. J. Modern Phys.* 17:41–47
- Landau L, Lifshitz E. 1959. Fluid mechanics. *Pergamon Press* :231
- Leclercq P, Bellan J. 2005. Direct numerical simulation of gaseous mixing layers laden with multicomponent-liquid drops: liquid-specific effects. *J. Fluid Mech.* 533:57–94
- Lohse D. 2017. *Private Communication*
- Lu J, Biswas S, Tryggvason G. 2006. A DNS study of laminar bubbly flows in a vertical channel. *Int. J. of Multiphase Flow* 32:643–660
- Lu J, Fernandez A, Tryggvason G. 2005. The effect of bubbles on the wall drag in a turbulent channel flow. *Phys. Fluids* 17:095102–1–12

- Lu J, Tryggvason G. 2006. Numerical study of turbulent bubbly downflows in a vertical channel. *Physics of Fluids* 18:103302 (10 pages)
- Lu J, Tryggvason G. 2008. Effect of bubble deformability in turbulent bubbly upflow in a vertical channel. *Physics of Fluids* 20:040701
- Lu J, Tryggvason G. 2013. Dynamics of nearly spherical bubbles in a turbulent channel upflow. *J. Fluid Mech.* 732:166–189
- Lundgren T. 2003. Linearly forced isotropic turbulence. *Annual Research Briefs* Center for turbulence Research, Stanford:461–473
- Madavan N, Deutsch S, Merkle C. 1984. Reduction of turbulent skin friction by microbubbles. *Phys. Fluids* 27:356–363
- Maffettone P, Minale M. 1998. Equation of change for ellipsoidal drops in viscous flow. *J. Non-Newtonian Fluid Mech.* 78:227–241
- Mashayek F. 1998. Droplet-turbulence interactions in low-mach-number homogeneous shear two-phase flows. *J. Fluid Mech.* 367:163–203
- Maxey M, Riley J. 1983. Equation of motion for a small rigid sphere in a nonuniform flow. *Phys. Fluids* 26:883–889
- Maxey MR. 2017. Simulation methods for particulate flows and concentrated suspensions. *Annu. Rev. Fluid Mech.* 49:171–193
- Mazzitelli I, Lohse D, Toschi F. 2003. On the relevance of the lift force in bubbly turbulence. *J. Fluid Mech.* 488:283–313
- Miller R, Bellan J. 1999. Direct numerical simulation of a confined three-dimensional gas mixing layer with one evaporating hydrocarbon-droplet laden stream. *J. Fluid Mech.* 384:293–338
- Njobuenwu DO, Fairweather M. 2015. Dynamics of single, non-spherical ellipsoidal particles in a turbulent channel flow. *Chem. Eng. Sci.* 123:265–282
- Osher S, Fedkiw R. 2001. Level set methods: An overview and some recent results. *J. Comp. Physics* 169:463–502
- Prosperetti A. 1981. Motion of two superposed viscous fluids. *Phys. Fluids* 24:1217–1223
- Prosperetti A. 2017. Vapor bubbles. *Annu. Rev. Fluid Mech.* 49:221–248
- Qian D, McLaughlin J, Sankaranarayanan K, Sundaresan S, Kontomaris K. 2006. Simulation of bubble breakup dynamics in homogeneous turbulence. *Chem. Eng. Comm.* 193:1038–1063
- Qian Y, d’Humières D, Lallemand P. 1992. Lattice BGK models for Navier-Stokes equation. *Europhys. Lett.* 17:479–484
- Reeks MW. 1983. The transport of discrete particles in inhomogeneous turbulence. *J. Aerosol Sci.* 14:729–739
- Risso F, Fabre J. 1998. Oscillations and breakup of a bubble immersed in a turbulent field. *J. Fluid Mech.* 806:323–355
- Roccon A, Paoli MD, Zonta F, Soldati A. 2017. Viscosity-modulated breakup and coalescence of large drops in bounded turbulence. *Phys. Rev. Fluids* 2:083603–1–13
- Russo E, Kuerten JGM, van der Geld CWM, Geurts BJ. 2014. Water droplet condensation and evaporation in turbulent channel flow. *J. Fluid Mech.* 749:666–700
- Saffman P. 1965. The lift on a small sphere in a slow shear flow. *J. Fluid Mech.* 22:385–400
- Saffman PG, Turner J. 1956. On the collision of drops in turbulent clouds. *J. Fluid Mech.* 1:16–30
- Sankaranarayanan K, Kevrekidis I, Sundaresan S, Lu J, Tryggvason G. 2003. A comparative study of lattice Boltzmann and front-tracking finite-difference methods for bubble simulations. *Int. J. of Multiphase Flow* 29:109–116
- Scarbolo L, Bianco F, Soldati A. 2015. Coalescence and breakup of large droplets in turbulent channel flow. *Phys. Fluids* 27:073302–1–12
- Scarbolo L, Bianco F, Soldati A. 2016. Turbulence modification by dispersion of large deformable droplets. *European Journal of Mechanics B-Fluids* 55:294–299
- Scarbolo L, Molin D, Perlekar P, Sbragaglia M, Soldati A, Toschi F. 2013. Unified framework for a side-by-side comparison of different multicomponent algorithms: Lattice Boltzmann vs. phase

- field model. *J. Comp. Physics* 234:263–279
- Scarbolo L, Soldati A. 2013. Turbulence modulation across the interface of a large deformable drop. *Journal of Turbulence* 14:27–43
- Scardovelli R, Zaleski S. 1999. Direct numerical simulation of free-surface and interfacial flow. *Annu. Rev. Fluid Mech.* 31:567–603
- Shan X, Chen H. 1993. Lattice Boltzmann model for simulating flows with multiple phases and components. *Phys. Rev. E.* 47:1815–1819
- Shardt O, Derksen J, Mitra S. 2013. Simulations of droplet coalescence in simple shear flow. *Langmuir* 29:6201–6212
- Snyder M, Knio O, Katz J, Le Maitre O. 2007. Statistical analysis of small bubble dynamics in isotropic turbulence. *Phys. Fluids* 19:065108–1–25
- Spandan V, Lohse D, Verzicco R. 2016. Deformation and orientation statistics of neutrally buoyant sub-kolmogorov ellipsoidal droplets in turbulent Taylor-Couette flow. *J. Fluid Mech.* 809:480–501
- Spandan V, Meschini V, Ostilla-Mnicoc R, Lohse D, Querzoli G, et al. 2017a. A parallel interaction potential approach coupled with the immersed boundary method for fully resolved simulations of deformable interfaces and membranes. *J. Comp. Physics* 348:567–590
- Spandan V, Verzicco, Lohse D. 2018. Physical mechanisms governing drag reduction in turbulent Taylor-Couette flow with finite-size deformable bubbles. *J. Fluid Mech.* submitted
- Spandan V, Verzicco R, Lohse D. 2017b. Deformable ellipsoidal bubbles in Taylor-Couette flow with enhanced Euler-Lagrangian tracking. *Phys. Rev. Fluids* 2:104304
- Sugiyama K, Calzavarini E, Lohse D. 2008. Microbubbly drag reduction in Taylor-Couette flow in the wavy vortex regime. *J. Fluid Mech.* 608:21–41
- Sun Y, Beckermann C. 2007. Sharp interface tracking using the phase-field equation. *J. Comp. Physics* 220:626–653
- Sussman M, Puckett E. 2000. A coupled level set and volume-of-fluid method for computing 3d and axisymmetric incompressible two-phase flows. *J. Comp. Physics* 162:301–337
- Sussman M, Smereka P, Osher S. 1994. A level set approach for computing solutions to incompressible two-phase flow. *J. Comp. Physics* 114:146–159
- Swift M, Orlandini E, Osbornand WR, Yeomans JM. 1996. Lattice boltzmann simulations of liquid-gas and binary fluid systems. *Phys. Rev. E.* 54:5041–5052
- Tryggvason G, Bunner B, Esmaeeli A, Juric D, Al-Rawahi N, et al. 2001. A front-tracking method for the computations of multiphase flow. *J. Comp. Physics* 169:708–759
- Tryggvason G, Dabiri S, Aboulhasanzadeh B, Lu J. 2013. Multiscale considerations in direct numerical simulations of multiphase flows. *Phys. Fluids* 25:031302–1–13
- Tryggvason G, Esmaeeli A, Lu J, Homma S, Biswas S. 2006. Recent progress in computational studies of disperse bubbly. *Multiphase Science and Technology* 18:231–249
- Unverdi S, Tryggvason G. 1992. A front-tracking method of viscous incompressible, multi-fluid flows. *J. Comp. Physics* 100:25–37
- van der Veen R, Huisman S, Merbold S, Harlander U, Egbers C, et al. 2016. Taylor-Couette turbulence at radius ratio  $\eta = 0.5$ : scaling, flow structures and plumes. *J. Fluid Mech.* 799:334–351
- Vanella M, Balaras E. 2009. A moving-least-squares reconstruction for embedded-boundary formulations. *J. Comp. Physics* 228:6617–6628
- Wang LP, Maxey MR. 1993. The motion of microbubbles in a forced isotropic and homogeneous turbulence. *Appl. Sci. Res.* 51:291–296
- Yue P, Zhou C, Feng J. 2007. Spontaneous shrinkage of drops and mass conservation in phase-field simulations. *J. Comp. Physics* 223:1–9